Cell Reports

Article

Essential Roles of Cohesin STAG2 in Mouse Embryonic Development and Adult Tissue Homeostasis

Graphical Abstract

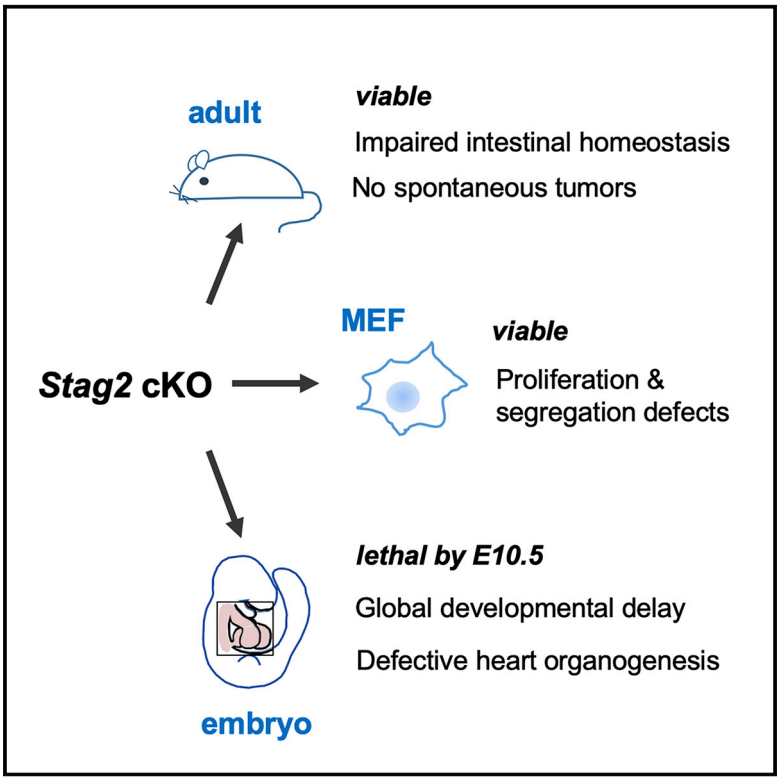

Highlights

- MEFs lacking STAG2 show reduced proliferation and mild cohesion defects
- Stag2 loss in adult mice reduces fitness but does not increase tumor incidence
- Stag2 KO embryos die by E10.5 with global developmental delay and malformed hearts

Authors

Magali De Koninck, Eleonora Lapi, Claudio Badía-Careaga, ..., Miguel Manzanares, Francisco X. Real, Ana Losada

Correspondence

alosada@cnio.es

In Brief

Cells carry STAG1- and STAG2-cohesin complexes whose functional specificity remains unclear. De Koninck et al. show that *Stag2* deletion in mice results in embryonic lethality by mid-gestation. In contrast, STAG2 is not strictly required for viability in cells or adult tissues, and its loss is not sufficient to elicit tumorigenesis.

De Koninck et al., 2020, Cell Reports *32*, 108014
August 11, 2020
https://doi.org/10.1016/j.celrep.2020.108014

CellPress

Cell Reports

CellPress
OPEN ACCESS

Article

Essential Roles of Cohesin STAG2 in Mouse Embryonic Development and Adult Tissue Homeostasis

Magali De Koninck,[1,7] Eleonora Lapi,[2,3,7] Claudio Badía-Careaga,[4,7] Itziar Cossío,[4] Daniel Giménez-Llorente,[1] Miriam Rodríguez-Corsino,[1] Elena Andrada,[2] Andrés Hidalgo,[4] Miguel Manzanares,[4,5] Francisco X. Real,[2,3,6] and Ana Losada[1,8,*]

[1]Chromosome Dynamics Group, Molecular Oncology Programme, Spanish National Cancer Research Centre (CNIO), 28029 Madrid, Spain
[2]Epithelial Carcinogenesis Group, Molecular Oncology Programme, Spanish National Cancer Research Centre (CNIO), 28029 Madrid, Spain
[3]CIBERONC, Madrid, Spain
[4]Centro Nacional de Investigaciones Cardiovasculares (CNIC), 28029 Madrid, Spain
[5]Centro de Biología Molecular "Severo Ochoa" (CBMSO), CSIC-UAM, 28049 Madrid, Spain
[6]Departament de Ciències Experimentals i de la Salut, Universitat Pompeu Fabra, 08003 Barcelona, Spain
[7]These authors contributed equally
[8]Lead Contact
*Correspondence: alosada@cnio.es
https://doi.org/10.1016/j.celrep.2020.108014

SUMMARY

Cohesin mediates sister chromatid cohesion and 3D genome folding. Two versions of the complex carrying STAG1 or STAG2 coexist in somatic vertebrate cells. *STAG2* is commonly mutated in cancer, and germline mutations have been identified in cohesinopathy patients. To better understand the underlying pathogenic mechanisms, we report the consequences of *Stag2* ablation in mice. STAG2 is largely dispensable in adults, and its tissue-wide inactivation does not lead to tumors but reduces fitness and affects both hematopoiesis and intestinal homeostasis. STAG2 is also dispensable for murine embryonic fibroblasts *in vitro*. In contrast, *Stag2*-null embryos die by mid-gestation and show global developmental delay and defective heart morphogenesis, most prominently in structures derived from secondary heart field progenitors. Both decreased proliferation and altered transcription of tissue-specific genes contribute to these defects. Our results provide compelling evidence on cell- and tissue-specific roles of different cohesin complexes and how their dysfunction contributes to disease.

INTRODUCTION

Cohesin is a four-subunit complex that holds the sister chromatids together to ensure faithful DNA repair by homologous recombination and proper chromosome segregation during cell division (Morales and Losada, 2018; Nasmyth and Haering, 2009). It is present in all cells, and its cohesive function is essential for proliferation. In addition, cohesin contributes to the spatial organization of the genome and to the activation and repression of tissue-specific transcriptional programs together with architectural proteins such as CTCF and transcriptional regulators like Mediator (Dowen et al., 2014; Faure et al., 2012; Kagey et al., 2010; Merkenschlager and Nora, 2016). In the cohesin complexes present in vertebrate somatic cells, the Structural Maintenance of Chromosomes (SMC) heterodimer of SMC1A and SMC3 associates with the kleisin subunit RAD21 and with one of the two versions of the Stromal Antigen (SA/STAG) subunit, namely, STAG1 or STAG2 (Losada et al., 2000). The two variants are present in all tissues and cell types, but their functional specificity is not well established (Cuadrado and Losada, 2020). We previously showed that genetic ablation of *Stag1* in mice is embryonic lethal, which indicates that the two complexes are not redundant, at least during embryonic development (Remeseiro et al., 2012a). Lethality starts after embryonic day 11.5 (E11.5), but a small fraction of embryos survive to E18.5 and present severe developmental delay and general hypoplasia (Remeseiro et al., 2012b).

In *Stag*1-null mouse embryonic fibroblasts (MEFs), telomere cohesion is impaired, preventing efficient replication of telomeres and causing chromosome segregation defects in mitosis (Remeseiro et al., 2012a). Centromere and arm cohesion are not clearly affected, which suggests that cohesin-STAG1 is specifically required for telomere cohesion, whereas cohesin-STAG2 contributes to cohesion in other chromosomal regions. Results in human cells are in line with these findings, although the extent of cohesion defects reported in the absence of STAG2 is variable (Canudas and Smith, 2009; Kim et al., 2016; van der Lelij et al., 2017; Mullenders et al., 2015). Specific contributions of cohesin-STAG2 to DNA replication and repair have also been reported (Kong et al., 2014; Meisenberg et al., 2019; Mondal

et al., 2019). In any case, a single variant is sufficient, and necessary, to maintain cell viability in culture (van der Lelij et al., 2017; Liu et al., 2018; Remeseiro et al., 2012a).

Cohesin variants also contribute distinctly to genome organization and gene regulation. In *Stag1*-null MEFs, cohesin distribution and their transcriptome are altered (Remeseiro et al., 2012b). In the pancreas of heterozygous *Stag1* mice, the architecture of the *Reg* locus and the transcription of some of its genes are also changed compared with those in the pancreas of wild-type (WT) littermates, suggesting that STAG2 is not sufficient to compensate for the reduced levels of STAG1 (Cuadrado et al., 2015). In human mammary epithelial cells, downregulation of STAG1 or STAG2 results in distinct changes in gene expression and chromatin contacts (Kojic et al., 2018). Cohesin-STAG1 and cohesin-STAG2 colocalize with CTCF and play a major role in the preservation of topologically associating domain (TAD) borders. In contrast, cohesin-STAG2 is also present at enhancers lacking CTCF that are bound by other transcriptional regulators (Cuadrado et al., 2019; Faure et al., 2012; Kojic et al., 2018; Sasca et al., 2019) Importantly, cohesin-STAG1 cannot occupy these non-CTCF cohesin sites even when STAG2 is absent (Kojic et al., 2018). Specific distribution of the two cohesin variants has also been reported in hematopoietic stem cells (HSCs), in which the loss of STAG2 decreases the transcription of lineage-specification genes and promotes stem cell renewal (Viny et al., 2019). In mouse embryonic stem cells, cohesin-STAG2 promotes compaction of Polycomb domains and the establishment of long-range interaction networks between distant Polycomb-bound promoters that are important for gene repression (Cuadrado et al., 2019).

Germline mutations in genes encoding cohesin and its regulatory factors are at the origin of a group of human syndromes collectively known as cohesinopathies. Cornelia de Lange syndrome (CdLS) is the most common of them, and up to 60% of the patients carry heterozygous mutations in *NIPBL*, a protein involved in loading cohesin on chromatin (Liu et al., 2009; Sarogni et al., 2020). Clinical features often include growth retardation, intellectual disability, facial dysmorphism, and congenital heart defects. Recently, germline mutations in *STAG1* and *STAG2* have been identified in patients with features partially overlapping those of CdLS and other cohesinopathies (Lehalle et al., 2017; Mullegama et al., 2019; Soardi et al., 2017; Yuan et al., 2019). Somatic mutations in cohesin genes, particularly in *STAG2*, have also been identified in several tumor types (De Koninck and Losada, 2016). *STAG2* has been recognized as one of the 12 genes significantly mutated in 4 or more cancer types (Lawrence et al., 2014). Among them, STAG2 loss is most frequent in urothelial bladder cancer (Balbás-Martinez et al., 2013; Taylor et al., 2014). The evidence emerging from the study of diseases associated with both germline and somatic cohesin mutations strongly suggests that gene deregulation, rather than defects in chromosome segregation, underlies the pathogenic mechanism (Balbás-Martinez et al., 2013; Liu et al., 2009; Mullenders et al., 2015).

Given the growing importance of *STAG2* in human disease, we generated a *Stag2* conditional knockout (cKO) mouse strain to identify specific functions of STAG2 at the cellular and organismal levels.

RESULTS

Mild Cohesion Defects and Slower Proliferation in STAG2-Deficient MEFs

First, we generated a cKO allele of the *Stag2* gene, which is located on the X chromosome (Figure S1). Next, *Stag2* cKO MEFs were isolated from E12.5 embryos resulting from mating $Stag2^{lox/lox}$ females with males carrying *hUBC-CreERT2* for ubiquitous, tamoxifen-induced activation of the Cre recombinase. Upon addition of 4-hydroxy-tamoxifen (4-OHT) to the culture medium, STAG2 protein levels in treated MEFs (KO) dropped below 5% of the amount present in untreated MEFs (WT), and compensatory upregulation of STAG1 could be observed (Figure 1A). The doubling time of STAG2-deficient cells was higher than the WT (Figure 1B), but flow cytometry analysis did not reveal differences in the cell cycle profiles of WT and KO MEFs (Figure 1C). A statistically significant increase in the percentage of caspase-3-positive cells was observed in the KO MEF cultures (14% versus 3% in WT MEFs; Figure 1D), suggesting a contribution of cell death to the higher doubling time. We next examined sister chromatid cohesion and chromosome segregation. For these experiments, *Stag2* was deleted under serum-starved conditions, and cells going through the first mitosis after release from the G0 arrest were collected. Very few cases of severe cohesion defects (i.e., complete sister chromatid unpairing) were detected in metaphase spreads from WT or KO MEFs (1.3% and 3% of chromosomes per metaphase examined, respectively; Figure 1E, bottom left). However, we did observe a larger fraction of chromosomes with mild cohesion defects (i.e., increased distance between sister centromeres; 26% in KO versus 11% in WT MEFs; Figure 1E, bottom right). We also found a ca. 2-fold increase in the percentage of anaphase cells with lagging chromosomes and/or chromosome bridges among KO MEFs compared with that of WT MEFs (29% versus 17%), although the difference did not reach statistical significance (Figure 1F). Finally, we observed that the proportion of metaphases with an abnormal chromosome number increased the longer MEFs were grown in the absence of STAG2 (Figure 1G). Overall, these defects are milder than those identified in *Stag1*-null MEFs (Remeseiro et al., 2012a) or in C2C12 myoblasts or HeLa cells after STAG2 downregulation by small interfering RNA (siRNA) (Canudas and Smith, 2009; Remeseiro et al., 2012a). We conclude that primary cultured cells almost completely lacking STAG2 can proliferate, although at slower rates. They maintain sufficient cohesion to divide successfully but mis-segregate chromosomes more frequently that WT cells.

STAG2 Inactivation in Adult Mice Does Not Lead to Spontaneous Tumors

To determine whether STAG2 is essential in adulthood, male and female 4-week-old *Stag2* cKO mice carrying or not carrying the *hUBC-CreERT2* transgene (hereafter referred to as KO and WT, respectively) were fed with a tamoxifen-containing diet (TMX). We did not observe an acute loss of viability in the KO mice, but long-term follow up revealed that their survival was significantly shorter than that of WT mice (Figure 2A). At 12 weeks, loss of the STAG2 protein was confirmed in a large fraction of cells (> 80%) in all tissues from KO mice analyzed by

CellPress
OPEN ACCESS

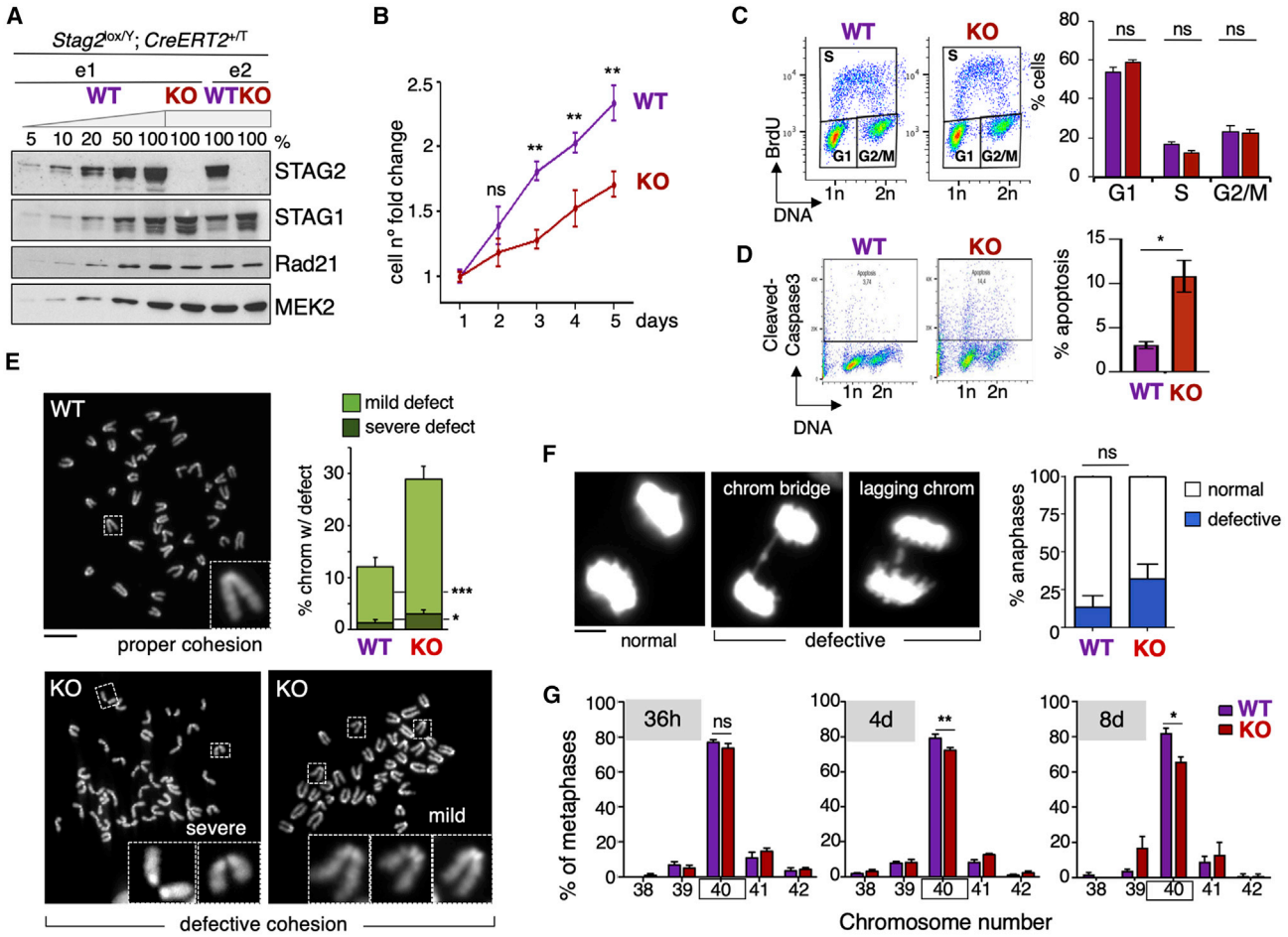

Figure 1. STAG2-Deficient MEFs Display Slower Proliferation and Increased Rates of Chromosome Missegregation

(A) Immunoblot analyses of whole-cell extracts of *Stag2*-cKO MEFs from two embryos (e1 and e2) untreated or treated for 4 days with 4-OHT (WT and KO hereafter). Decreasing amounts (shown as % of maximal) of WT MEF extract were loaded to estimate STAG2 depletion levels. MEK2 is used as a loading control.

(B) Growth curves of WT and KO MEFs representing the average fold increase in cell number relative to the number of cells seeded on day 1. Data are from MEFs from 2 embryos, each analyzed in triplicates (mean ± SEM).

(C) Representative BrdU incorporation profiles by fluorescence-activated cell sorting (FACS) in WT and KO MEFs, and bar graph showing values for n = 4 (mean ± SEM).

(D) Representative FACS profiles of cleaved caspase 3 staining in WT and KO MEFs, and bar graph showing the fraction of apoptotic cells in n = 3 (mean ± SEM).

(E) Representative metaphase spreads from *Stag2*-WT and -KO MEFs, and quantification (mean ± SEM) of chromosomes showing centromeric cohesion defects (severe or mild) At least 100 metaphases from MEFs from 3 different embryos were inspected. Scale bar, 10 μm.

(F) Images of normal and defective anaphase cells found among WT and KO MEFs (left), and their quantification (right, mean ± SEM). At least 100 anaphases from MEFs from 3 different embryos were inspected. Scale bar, 5 μm.

(G) Quantification of chromosome number frequency in metaphase spreads of WT and KO MEFs (mean ± SEM). For the first time point, MEFs were serum starved for 3 days in ± 4-OHT and released for 36 h to reach the first mitosis; "4d" and "8d" indicate number of days asynchronously growing MEFs were kept ± 4-OHT cells before analysis. At least 100 metaphases from MEFs from 3 different embryos were inspected. Mann-Whitney test; ***$p < 0.001$, **$p < 0.01$, *$p < 0.05$; ns, $p \geq 0.05$.

immunohistochemistry (Figure 2B, left panel; Figure 2C, first point in the graph). However, over time, the fraction of STAG2-negative cells dropped dramatically in the more proliferative tissues (e.g., intestine and spleen) and to a lesser extent in tissues with moderate (i.e., lymph node) or low proliferation rates (i.e., liver, pancreas or brain; Figure 2C; compare the labeling of STAG2 in the lymph node and the pancreas of a 35-week-old KO mouse in Figure 2B). These results suggest that recombination-mediated deletion of the *Stag2* gene is incomplete and disadvantageous to cells; as a consequence, WT unrecombined cells rapidly outcompete mutant cells in highly proliferative tissues. Similar results have been found in other genetic mouse models (Hay et al., 2005; Ireland et al., 2004). Given the proposed role of STAG2 as tumor suppressor, we searched for evidence of malignancy in the KO mice. There were no preneoplastic or neoplastic lesions in the full necropsies of KO mice (n = 13). Likewise, a macroscopic assessment failed to reveal neoplasms in a large cohort of mice (n = 63) of up to 70 weeks age, indicating

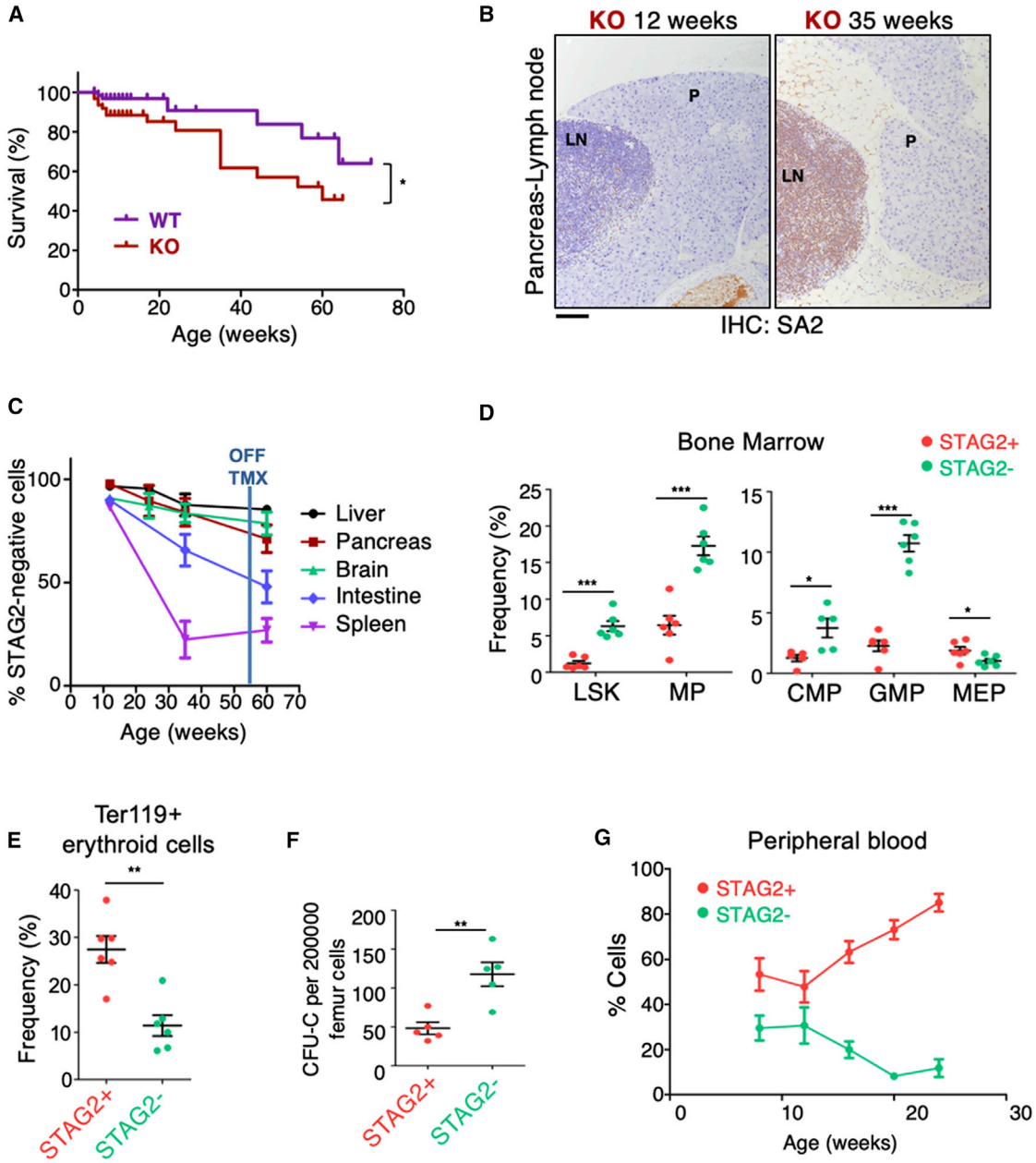

Figure 2. Effects of STAG2 Ablation in Adult Mice

(A) Kaplan-Meier survival curves of *Stag2*-KO and -WT mice. Four-week-old *Stag2*-cKO male and female mice carrying the *Cre-ERT2* allele (KO; n = 63), or not (WT; n = 66), were continuously fed on a TMX-containing diet and monitored thrice weekly. No sex differences in survival were observed. Gehan-Breslow-Wilcoxon test; *p < 0.05.

(B) Representative images of STAG2 expression in sections of pancreas (P) and associated lymph node (LN) of KO mice at 12 (left) and 35 (right) weeks of age, assessed by immunohistochemistry (IHC). Scale bar, 100 μm.

(C) Percentage of recombined STAG2-negative cells in various organs over time was assessed by IHC. Representative microphotographs were quantified with ImageJ software (3 micrographs per mouse; n = 3 to 6 mice depending on the time point). Error bars indicate SEM.

(D) Flow cytometry analysis of bone marrow HSPCs in 12-week-old KO mice (n = 6). Left, LSK (Lin− c-Kit+ Sca1+); MP (Lin− c-Kit+). Right, CMP (Lin− c-Kit+ CD34+ CD1632−); GMP (Lin− c-Kit+ CD34+ CD1632+); MEP (Lin− c-Kit+ CD34− CD1632−). Error bars indicate SEM. Unpaired t test; *p < 0.05; ***p < 0.001.

(E) Flow cytometry analysis of bone marrow Ter119+ cells in 12-week-old KO mice (n = 6). Error bars indicate SEM. Unpaired t test; **p < 0.01.

(F) Colony-forming unit assay using FACS-sorted GFP and Tomato total bone marrow cells from 12-week-old KO mice (n = 5). Error bars indicate SEM. Unpaired t test; **p < 0.01.

(G) Flow cytometry analysis of GFP+ (STAG2−) and Tomato+ (STAG2+) leukocytes in peripheral blood of KO mice over time (n = 5). Error bars indicate SEM.

that *Stag2* inactivation on its own does not increase spontaneous tumor incidence in adult mice.

STAG2 Supports Normal Hematopoiesis in Adult Mice

Compared with controls, KO mice treated with TMX for 8 weeks (starting at 4 weeks of age) displayed mild reductions in peripheral blood leukocyte, erythrocyte, and platelet counts, pointing to anomalies in hematopoiesis (Figures S2A and S2B). We took advantage of the dual-fluorescent Cre reporter (*Rosa26_ACTB-tdTomato_EGFP*) carried by the KO animals to study the relative abundance of the WT and KO hematopoietic populations: unrecombined WT cells display cell-membrane-localized tdTomato fluorescence, whereas Cre-recombinase-expressing cells and their progeny display membrane-localized EGFP fluorescence. Analyses of leukocytes from peripheral blood and spleen of KO animals carrying the *Stag2* cKO allele, the *hUBC-CreERT2* transgene, and the aforementioned Cre reporter revealed an enrichment in myeloid cells (monocytes and neutrophils) and a significant reduction in T lymphocytes among STAG2-deficient (GFP+) cells compared with that of unrecombined (Tomato+) cells (Figure S2C). To address whether this phenotype was due to a defect in hematopoiesis, we analyzed stem cell populations in the bone marrow. A clear expansion of the LSK (Lin− Sca1+ c-Kit+) population and myeloid progenitor (MP) compartment was associated with STAG2 loss (Figure 2D, left). Further analysis of MPs showed an increased frequency in common MPs (CMPs) and granulocyte-monocyte progenitors (GMPs) and a decrease in megakaryocyte-erythrocyte progenitors (MEPs) among STAG2-deficient (GFP+) cells, in agreement with the findings in peripheral blood (Figure 2D, right). Reductions in MEPs paralleled a decrease in bone marrow Ter119+ erythroid cells in KO mice (Figures 2E and S2D). Functional analyses revealed a higher colony-forming capacity of STAG2-deficient hematopoietic cells than that of WT (Figure 2F), which is concordant with the increase in LSK cells. The loss in lymphoid potential might explain the reduced chimerism of mutant cells over time in peripheral blood (Figure 2G). These results support the notion that STAG2 loss leads to increased self-renewal and to impaired differentiation of HSCs. We observe an increase in granulocyte and macrophage populations at the expense of the erythroid cells (myeloid skewing) and an overall competitive disadvantage when WT HSCs are present. These data are consistent with previous reports on the contribution of cohesin to normal hematopoiesis and the occurrence of cohesin mutations in myeloid malignancies (Mullenders et al., 2015; Thol et al., 2014; Viny et al., 2019). In contrast with the reduced proliferation of *Stag2* KO MEFs, the enhanced self-renewal of *Stag2* KO HSCs provides important evidence for supporting a STAG2 tumor suppressor role as well as possible tissue-specific effects of *Stag2* inactivation.

STAG2 Is Required for Intestinal Homeostasis

Shortly after the initiation of a TMX diet at 4 weeks, the survival curve of KO mice diverted from that of WT mice (Figure 2A), the former also showing reduced body weight (Figure 3A). Histological analyses of 8-week-old animals failed to reveal major alterations in tissues of KO mice with the exception of the intestine, in which patches of epithelial erosion and necrosis were observed. Moderate or severe lesions were present in 60% of mutant mice, whereas WT mice showed much milder and less abundant lesions (Figure 3B). We analyzed proliferation and apoptosis in the small bowel: intestinal crypts from KO mice showed a significant reduction of bromodeoxyuridine-positive (BrdU+) cells (Figure 3C), suggesting reduced regeneration capacity. In addition, and in agreement with the findings in cultured MEFs, we found a significant increase in apoptosis measured as active caspase-3 labeling (Figure 3D). To acquire further insight into the requirement of STAG2 for intestinal cell renewal, we generated primary organoid cultures from the small intestine of TMX-treated KO mice carrying the fluorescent reporter (Figure 3E, left). STAG2-null GFP+ cells yielded fewer and smaller organoids than STAG2 proficient Tomato+ cells (Figure 3E, right). From these findings, we conclude that STAG2 is also required for intestinal homeostasis.

Stag2-Null Embryos Display Developmental Delay by E9.5 and Die Soon Afterward

To assess the effect of *Stag2* inactivation in embryogenesis, *Stag2*$^{lox/lox}$ females were crossed with males carrying the *CAG-Cre* transgene, which codes for a Cre recombinase that is expressed ubiquitously from the zygote stage. Because *Stag2* is an X-linked gene, male embryos resulting from this cross would be either WT or null (KO) for *Stag2*, whereas females would be WT or heterozygous (see genotyping strategy in Figure S1D). There were no *Stag2*-null males among the offspring, whereas heterozygous females were born at sub-Mendelian ratio (Figure 4A, last column). To determine at what point during embryonic development STAG2 becomes essential, we extracted and genotyped litters at different times after conception. We found live KO male embryos at the expected Mendelian ratios at E8.5 and E9.5, but not later (Figure 4A). In all studies presented hereafter, we used exclusively male embryos, either WT or KO. Immunohistochemical analyses of embryo sections with STAG2-specific antibodies confirmed tissue-wide absence of the protein (Figure 4B). Importantly, E9.5 KO embryos were visibly smaller than their WT littermates with variable penetrance of the phenotype (mild and severe examples shown in Figure 4C). To establish whether the growth delay is accompanied by developmental delay, we counted somites along the dorsal axis of embryos extracted at E8.5, E9.5, and E10.5 (see detail in Figure 4C). Somite number provides a reliable readout of developmental stage between E8 and E10.5. Although all embryos presented similar somite counts by E8.5, a significantly reduced number of somites was observed in mutant embryos by E9.5. By E10.5, the difference in somite counts between WT and KO embryos was equivalent to a 1-day lag (Figure 4D). Thus, a loss of STAG2 causes a generalized developmental delay, noticeable by E9.5 with variable penetrance, and results in death by E10.5.

Aberrant Heart Morphogenesis in Stag2-Null Embryos

To identify developmental defects that could explain embryonic lethality, we analyzed the histology of E9.5 KO embryos with both mild and severe growth phenotypes (KO mild and KO severe, respectively) and compared them with two different types of WT controls: littermates (age-matched, WT1) and embryos from different litters but with the same number of somites

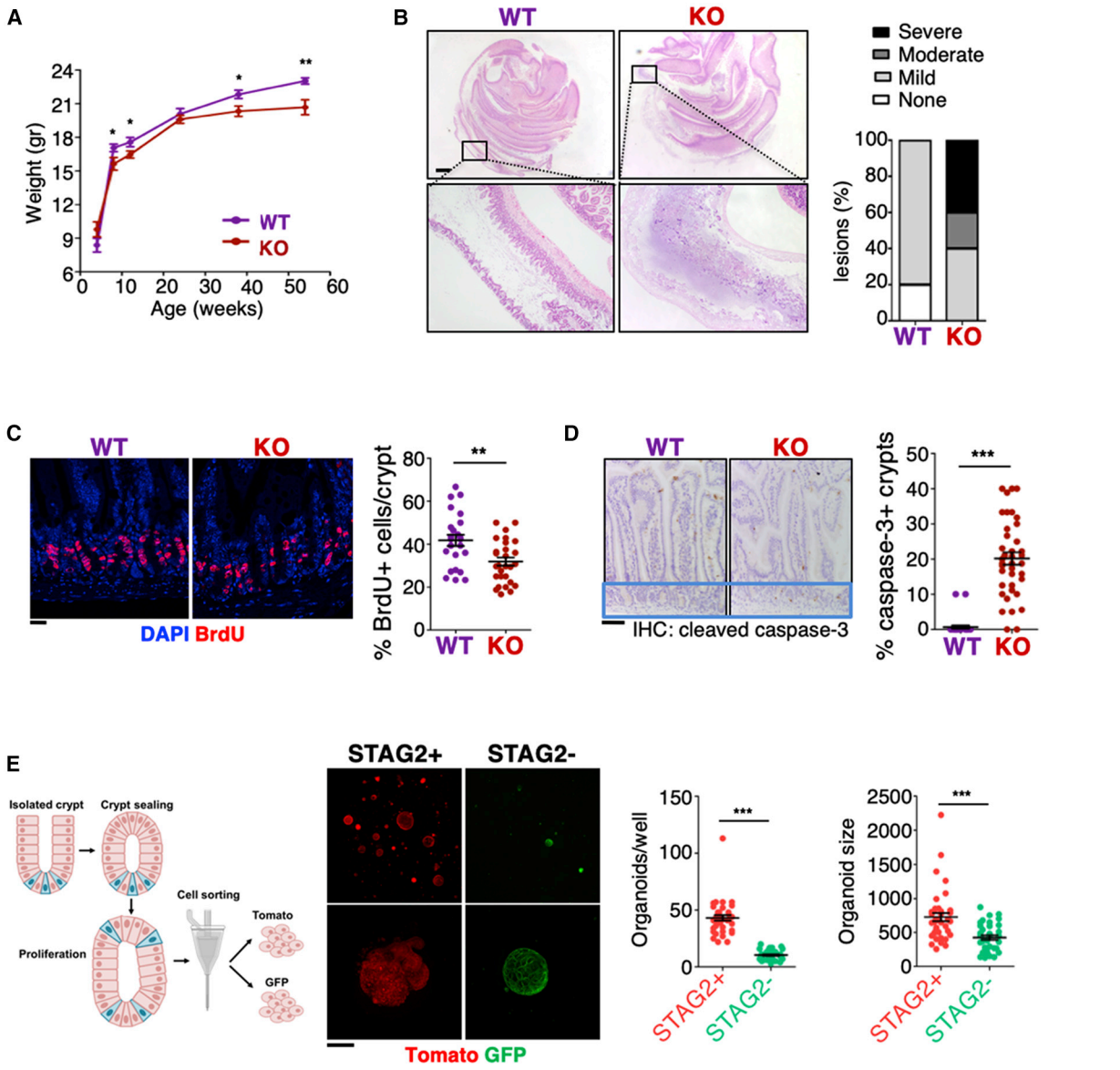

Figure 3. Requirement of STAG2 for Intestinal Cell Renewal

(A) Weight of KO and WT mice over time (n = 18, WT; n = 18, KO). Error bars indicate SEM. One-sided Mann-Whitney U test; *p < 0.05; **p < 0.01.

(B) Representative images of H&E-stained small intestine sections of 8-week-old WT and KO mice (left) and semiquantitative assessment of severity of lesions (right). Scale bar, 1 mm. (n = 5, WT; n = 5, KO).

(C) Immunofluorescence analysis of BrdU (red) in sections of 8-week-old WT and KO intestine. Nuclei are counterstained with 4′,6-diamidino-2-phenylindole (DAPI; blue). Scale bar, 25 μm. The percentage of BrdU+ cells per crypt is shown in the graph on the right (n = 24, WT; n = 29, KO). Error bars indicate SEM. Two-tailed Mann-Whitney U test; **p < 0.01.

(D) Immunohistochemical analysis of cleaved caspase-3 in sections of 8 week-old WT and KO intestine. Nuclei are counterstained with hematoxylin. Crypt region is indicated by a dashed box. Scale bar, 50 μm. The percentage of crypts per section showing cleaved caspase-3 staining is plotted on the right (n = 30, WT; n = 39, KO). Error bars indicate SEM. Two-tailed Mann-Whitney U test; ***p < 0.001.

(E) Experimental design for intestinal organoid generation (left). Confocal microscopy images of Tomato+ (STAG2+) and GFP+ (STAG2−) organoids (middle). Scale bar, 100 μm. Quantification of the number and size of organoids (in pixels) obtained from cells sorted from primary intestinal organoids (5,000 cells/well) (right). Error bars indicate SEM. Paired t test; ***p < 0.001.

(stage-matched, WT2). Although KO severe embryos showed aberrant morphology of several structures, most tissues and organs from KO mild embryos did not present obvious malformations but were clearly more similar to stage-matched than to age-matched controls (see neural tube [NT] in Figure 5; see other structures in Figure S3). A remarkable exception to this general trend was a selective defect in the developing heart. At E9.5, the murine heart presents a multichambered conformation as a

A

♀ *Stag2* $^{lox/lox}$ x ♂ *Stag2* $^{+/Y}$; CAG-Cre $^{+/T}$

genotype			E8.5		E9.5		E10.5		E12.5		born	
			%	n	%	n	%	n	%	n	%	n
♀	WT		30	12	25	29	28	15	34	25	35	32
♀	HET		12.5	5	22.5	26	24	13	33	24	16	15
♂	WT		32.5	13	22.5	26	20	11	27	20	49	45
♂	KO	alive	20	10	30	**35**	2	**1**	0	**0**	0	**0**
♂	KO	dead	0	0	0	0	26	14	6	4	0	0

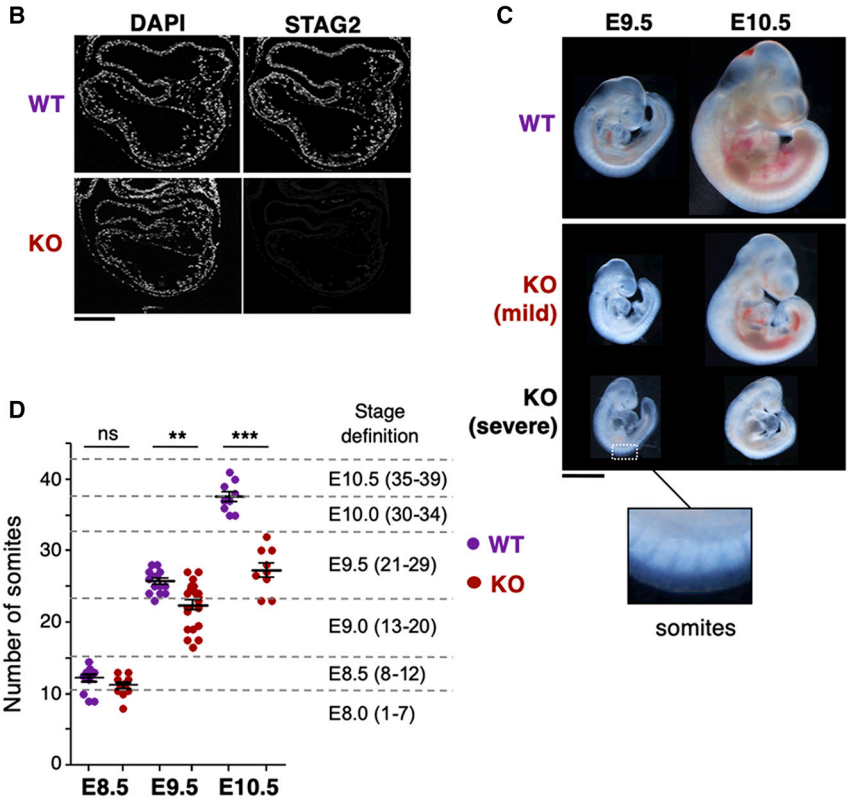

Figure 4. STAG2 Becomes Essential by Mid-gestation

(A) Viability of STAG2-deficient embryos at different stages of development. We genotyped 6, 14, 7, and 13 litters at E8.5, E9.5, E10.5, and E12.5, respectively, as well as 11 litters at weaning ("born"). Phenotypes and genotypes for *Stag2* are female WT (lox/+), female HET (Δ/+), male WT (lox/Y), male KO (Δ/Y).

(B) Immunofluorescence staining of STAG2 in transverse heart sections of WT and KO male embryos at E9.5. Nuclei are counterstained with DAPI. Scale bar, 200 μm.

(C) Representative images of WT and KO male embryos (mild and severe phenotypes) at E9.5 and E10.5. Scale bar, 1 mm. A detail of the somites apparent along the dorsal axis of the embryo is shown at the bottom.

(D) Somite counts of WT and KO male embryos: 6 litters at E8.5 (n = 13, WT; n = 10, KO), 9 litters at E9.5 (n = 19, WT; n = 25, KO), and 4 litters at E10.5 (n = 10, WT; n = 10, KO). Two-tailed Student's t test, ***$p < 0.001$, **$p < 0.01$; ns, $p \geq 0.05$. The number of somites expected at each stage of development is indicated on the right.

result of linear heart tube extension and looping (see scheme in Figure 5A). Two prospective ventricles and two prospective atria can be distinguished, although there is still no septation between them. The inflow tract (IFT) in the posterior pole of the heart tube allows blood to enter, and the outflow tract (OFT) is an extension of the ventricle that allows blood to flow out and will become the aorta and pulmonary trunk in an adult heart (Kelly et al. 2014). Histological analyses of serial heart sections (Figures 5A and 5B) revealed a smaller right ventricle (RV) in KO mild embryos than that in both controls, whereas no clear differences were found in the left ventricle (LV; compare images for WT1, KO mild, and WT2 under HCs [heart chambers] in Figure 5B). Quantification of the ventricular area confirmed this observation; although the RV was smaller in KO mild embryos than in both age- (WT1) and stage-matched (WT2) controls (Figure 5C), the LV was only smaller than age-matched controls (WT1) due to general developmental delay, but it was not different from stage-matched controls (WT2) (Figure 5D). The IFT of KO mild embryos appeared normal, but the OFT showed an aberrant rightward turning at the junction with the ventricular myocardium (white arrowhead in WT1 and KO mild under OFT in Figure 5B). Moreover, the length of the OFT was significantly reduced in KO mild embryos compared with that of both controls (Figure 5E). The defects described above were exacerbated in KO severe embryos, which displayed distended atria and ventricles with no visible indication of a future septum between right and left chambers (black arrowheads in WT1 and KO severe, under HC, in Figure 5B), and abnormal RV development (asterisk in Figure 5B). In these mutants, both the OFT and the IFT were distended. Unlike at E9.5, when penetrance was variable, all KO embryos displayed severe cardiac anomalies by E10.5, as well as extensive necrosis and apoptosis (Figure 5F). Thus, defective heart function may account for the embryonic lethality of *Stag2* KO embryos.

Decreased Proliferation in Stag2-Mutant Embryos

To shed light into the cellular mechanisms leading to the defects described above, we first confirmed that both STAG1 and STAG2 are expressed in the heart of E9.5 WT embryos by using immunofluorescence (Figure S4). These findings are consistent with reported data from single-cell RNA sequencing (RNA-seq) of E8.25 murine embryos, which shows similar patterns of

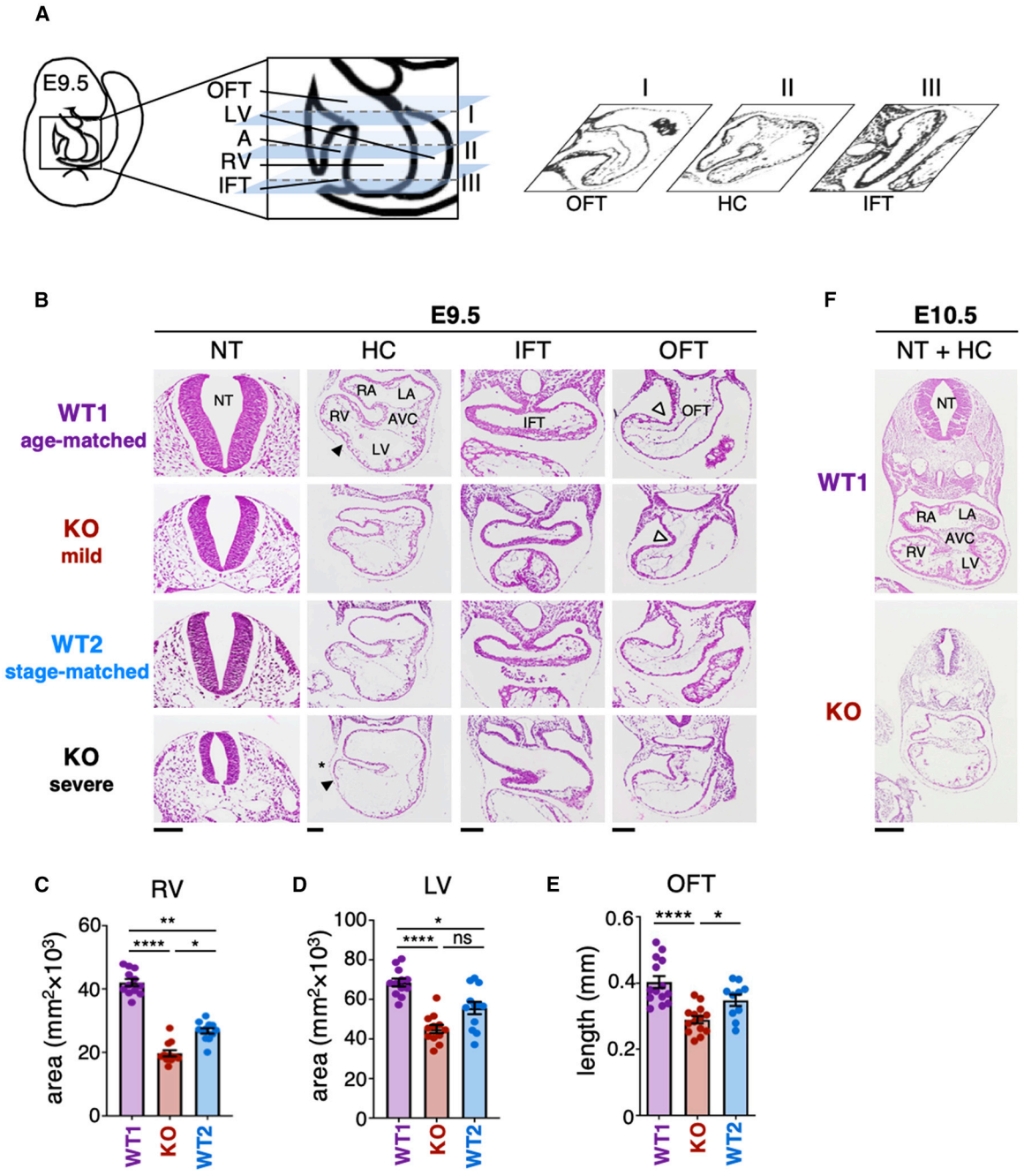

Figure 5. Heart Defects in *Stag2*-Mutant Embryos

(A) Scheme showing the different regions of an E9.5 embryonic heart and the approximate position and orientation of the transverse sections used for analysis in (B).

(B) H&E-stained sections of KO (mild and severe), WT1 (age-matched control), and WT2 (stage-matched control) E9.5 male embryo neural tube (NT), heart chambers (HCs), inflow tract (IFT), and outflow tract (OFT). RA, right atrium; LA, left atrium; AVC, atrioventricular canal; RV, right ventricle; LV, left ventricle. Black arrowheads indicate the position of the prospective septum between right and left chambers. White arrowheads point at the OFT curve. Asterisk highlights the small size of the RV in the KO severe embryo. Scale bars (valid for entire column), 100 μm.

(C) RV size measured in H&E-stained sections (12 sections from 4 embryos per genotype) from E9.5 WT1 (age-matched control), KO (mild), and WT2 (stage-matched control) male embryos. Mean ± SEM are shown. Kruskal-Wallis test and Dunn's multiple comparison post-test; ***$p < 0.001$, **$p < 0.01$, *$p < 0.05$; ns, $p \geq 0.05$.

(legend continued on next page)

expression for both genes (Ibarra-Soria et al., 2018). We next analyzed proliferation and apoptosis in E9.5 WT1, WT2, and KO mild embryos to uncover primary defects. Heart sections, as well as sections containing the NT for comparison, were labeled with anti-phosphohistone H3 (H3P) to detect proliferating cells and with Terminal deoxynucleotidyl transferase deoxyuridine triphosphate (dUTP) nick end labeling (TUNEL) to mark apoptotic cells. To better identify the different heart compartments, co-staining of Islet 1 (ISL1) was used. ISL1 is a transcription factor expressed in anterior and posterior secondary heart field (ASHF and PSHF, respectively) progenitors that is progressively turned off in their descendants as they migrate into, and populate, the heart tube through its anterior and posterior ends (OFT and IFT, respectively; see scheme in Figure S5A; Cai et al., 2003). The fraction of H3P-positive cells in the HCs (atria and ventricles) was significantly lower in the mutants than in their littermate age-matched WT1 controls but was similar to WT2 stage-matched controls (HC in Figures 6A, 6B, and S5B). These differences were reproduced in ASHF and OFT, as well as in the NT, whereas they were less prominent in PSHF and IFT (Figures 6A and 6B; Figure S5B). There was also increased apoptosis in mutant NT and HCs compared with that of both controls, although the number of TUNEL-positive cells was very low in all cases and inter-individual variability was high (Figure 6C). These results suggest that the global developmental delay observed in *Stag2* mutants at E9.5 is mainly due to a decrease in the proliferative capacity of mutant cells.

Specific Defects in Secondary Heart Field Progenitors in Stag2-Mutant Embryos

Although decreased proliferation might account for the global growth delay observed in the heart (and other organs) in mutant embryos, it failed to explain why morphological defects were more evident in certain heart structures, i.e., the OFT and RV. Interestingly, these structures derive from second heart field (SHF) progenitors, whereas the LV derives from the first heart field (FHF) progenitors (Kelly et al., 2014). More specifically, ISL1+ progenitors present in the ASHF migrate into the heart tube contributing to the OFT and RV (Figure S5A). We reasoned that the reduced size of RV and OFT length observed in mutant embryos compared with stage-matched WT2 controls (Figures 5C and 5E) could result from altered migration of ASHF progenitors (ISL1+) into the OFT. To test this possibility, we quantified total cell numbers in heart sections as well as in the NT. We found that in the NT, HC, and OFT, cellularity of KO mild embryos was lower than that in WT1 and more similar to WT2 embryos (Figure 6D), consistent with their smaller size (Figure 5) and reduced proliferation rates (Figure 6B). In contrast, cell numbers in the ASHF were similar in KO and WT1 littermates (Figure 6D), despite mutants showing a much reduced proliferation rate (Figure 6B). Moreover, although the fraction of ISL1+ progenitors in ASHF was similar in all embryos, it decreased in the OFT of KO mild embryos compared with that of both controls (Figure 6E). Thus, impaired migration of ASHF progenitors into the heart tube could explain the morphological defects in RV and OFT observed in mutant hearts.

Altered Transcription of Cardiac Development Regulators in Stag2-Mutant Embryos

To address whether gene regulation by cohesin could contribute to the phenotypes described above, we compared the heart transcriptomes of E9.5 *Stag2*-KO and -WT embryos by RNA-seq. To exclude variation related to developmental stage, we selected littermate embryos of both genotypes with a similar number of somites. To identify tissue-specific changes, we extracted RNA from the heart and from the NT lying adjacent to the heart. There were 1,881 differentially expressed genes (DEGs; false discovery rate [FDR] < 0.05) between WT samples of the two tissues, which we used to define a cardiac-enriched and a neural-enriched gene set (1,116 and 765 genes, respectively). Gene Ontology analysis confirmed the functional specificity of these gene sets (“cardiac” and “neural” genes, for simplicity; Figure 7A; Table S1). STAG2 loss had a greater impact on the heart transcriptome, as shown in the heatmap (Figure 7A). Accordingly, pairwise comparisons between WT and KO samples for each tissue identified 846 DEGs in the heart but only 5 in the NT (FDR < 0.05; Figure 7B; Table S2). Among the DEGs in the heart, there were 222 and 112 genes from the cardiac and neural gene sets, respectively, indicating that tissue-specific genes were preferentially affected by STAG2 loss (Figure 7C; Table S1). Moreover, among heart DEGs, most cardiac genes were downregulated, whereas the neural genes were upregulated (Figure 7D). These findings agree with the proposed role of cohesin-STAG2 in tissue-specific transcription, promoting the activation of genes specifying a tissue (i.e., cardiac genes in heart) and repression of alternative gene programs (e.g., neural genes in heart) (Kojic et al., 2018). A closer look at the list of DEGs in the heart revealed several cardiomyocyte markers and well-established SHF regulators among the downregulated genes (Figure 7B, right). For instance, Fgf8 and Hand2 contribute to the survival of ASHF progenitors, whereas Wnt5a activity is critical for their deployment into the OFT (Park et al., 2006; Sinha et al., 2015; Tsuchihashi et al., 2011), consistent with the defects described in the previous section. These data suggest that the loss of STAG2 alters the expression of genes encoding important regulators of heart remodeling by SHF progenitors. This finding, together with decreased proliferation, likely contributes to the observed defects in heart morphogenesis.

DISCUSSION

A major challenge in cohesin biology is to understand the specific functions of STAG1 and STAG2 (Cuadrado et al., 2019; Kojic et al., 2018; Wutz et al., 2020). To address this question, we

(D) LV size, as in (C).
(E) The outer curve of the OFT was measured in 10–12 sections from 4 embryos of each genotype stained as shown in Figure 6. Mean ± SEM are shown. Kruskal-Wallis test and Dunn’s multiple comparison post-test; ***$p < 0.001$, *$p < 0.05$; ns, $p \geq 0.05$.
(F) H&E-stained transverse sections encompassing the NT and the heart of a WT and a KO male embryo at E10.5. Heart regions indicated as in (A). Scale bar, 250 μm.

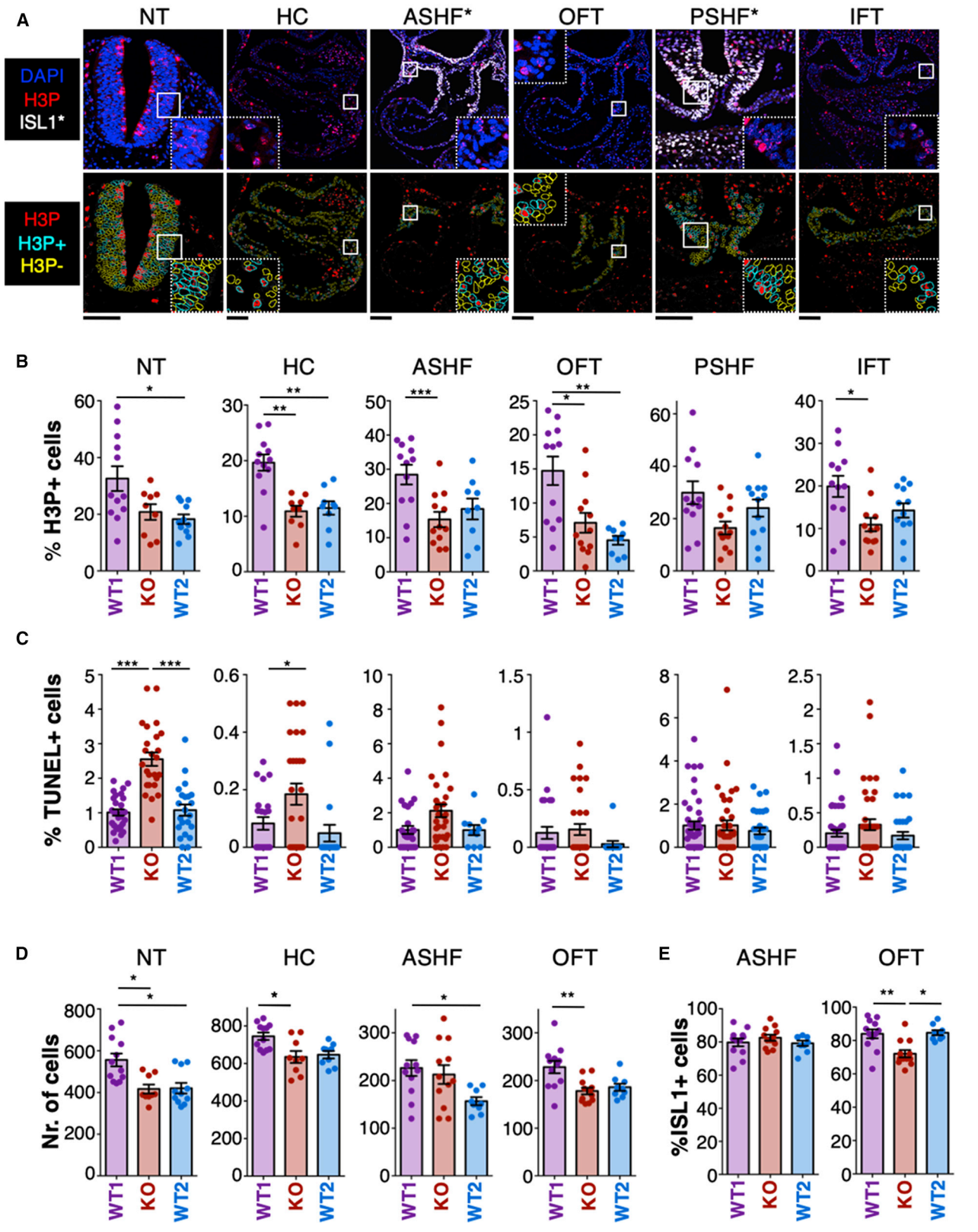

(legend on next page)

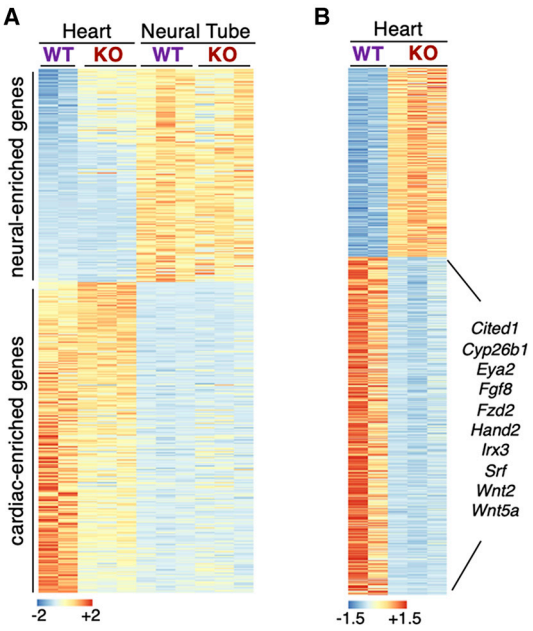

Figure 7. Transcriptional Deregulation in *Stag2*-Null Embryos

(A) Heatmap showing relative expression of 1,116 cardiac- and 765 neural-enriched genes in all samples. Gene sets were defined by differential expression between WT heart and WT NT samples.

(B) Heatmap of 846 DEGs in WT and KO heart samples. Among the downregulated genes, we highlight some with established roles in cardiomyocyte differentiation and SHF progenitors.

(C) Expected versus observed number of cardiac and neural genes found among heart DEGs. Total number of expressed genes was 21,653. Fisher's exact test; **** < 0.0001 ($p < 2E-12$).

(D) Boxplot of expression changes in the cardiac and neural genes identified as DEGs in the heart. See also Table S1.

previously characterized a *Stag1*-KO mouse (Remeseiro et al., 2012a, 2012b), and we have now generated a *Stag2*-KO mouse. Recently, a study describing the consequences of *Stag2* ablation in the hematopoietic system of adult mice demonstrated a specific role for STAG2 in balancing self-renewal and differentiation in hematopoietic precursors (Viny et al., 2019). Here, we describe instead the consequences of ubiquitous STAG2 elimination in embryos and adult mice.

Whole-body deletion of *Stag2* in young mice does not result in acute loss of viability, which suggests that STAG1 can largely compensate for the lack of STAG2 postnatally. Efficiency of Cre-mediated recombination of the *Stag2*-cKO allele was high in adult tissues 8 weeks after Cre induction, but the fraction of recombined cells decreased notably over the subsequent weeks in proliferative tissues despite continuous TMX administration. This observation indicates a clear proliferative disadvantage of STAG2-deficient cells and does not allow us to rule out that a more severe phenotype might be disclosed upon achieving a more complete or sustained depletion of STAG2. Consistent with results obtained upon *Stag2* deletion in HSCs by using *Mx1-Cre*, ubiquitous deletion results in increased self-renewal and defective lineage commitment in this compartment (Viny et al., 2019). Our histopathological analyses also detected defects in gastrointestinal tract homeostasis. This phenotype could result from a decreased proliferation capacity of the mutant cells, as suggested by our findings using organoids, and/or from altered regulation of the balance between self-renewal and differentiation in the intestine, as shown in HSCs. In fact, a recent study shows that cohesin promotes repression of differentiation genes in *Drosophila* intestinal stem cells to maintain stemness and intestinal homeostasis (Khaminets et al., 2020). However, TMX toxicity in the gut has been reported and was focused specifically in the stomach (Keeley et al., 2019). Thus, toxicity resulting from continued TMX administration—a condition used here to avoid expansion of unrecombined *Stag2* WT cells—may also contribute to the intestinal phenotype. A more detailed analysis of the effects of STAG2 loss in the intestine, by using a variety of TMX administration protocols and a time course, is warranted.

In contrast to the redundancy and functional compensation of the STAG proteins in adult mice, embryos require both proteins to complete development. Constitutive inactivation of *Stag1* in the germline is embryonic lethal and causes severe development delay, with incomplete penetrance, but no obvious organ malformation (Remeseiro et al., 2012a, 2012b). In contrast, inactivation of *Stag2* in the germline leads to earlier lethality, starting at E9.5. This phenotype is associated with a general developmental delay and a dramatic effect on heart development with no *Stag2*-null embryos surviving beyond E10.5. Histopathological characterization of KO mild embryos revealed specific defects in heart structures derived from the SHF, the RV, and OFT. More detailed analyses detected an accumulation of progenitor

Figure 6. Reduced Cell Proliferation and Impaired Migration of ASHFs in the Developing Heart of *Stag2*-Null Embryos

(A) Representative transverse sections of H3P staining of E9.5 WT1 embryos. Top row: original immunofluorescence signal of DAPI (blue), H3P (red), and ISL1 (white, only shown in regions marked with *). Both morphological criteria and ISL1 staining were used to demarcate ASHF and PSHF regions. Bottom row: H3P signal converted to a binary image, with representation of nuclei selection. Similar images for KO and WT2 embryos are shown in Figure S5. Scale bars, 100 μm.

(B) Quantification of H3P-positive cells as readouts for proliferation in E9.5 male embryos. A total of 9–12 non-consecutive sections from 3–4 embryos were analyzed per genotype and region.

(C) Quantification of TUNEL-positive cells as readouts for apoptosis in the same embryos. At least 10 sections from 3–4 embryos were analyzed per genotype and region.

(D and E) Quantification of the total number of cells per section (D) and ISL1-positive cells (E) in the indicated regions. Same sections as in (B) were analyzed. For (B)–(D), mean ± SEM are shown. Kruskal-Wallis test and Dunn's multiple comparison post-test; ***$p < 0.001$, **$p < 0.01$, *$p < 0.05$; ns, $p \geq 0.05$.

(ISL1+) cells in the ASHF of mutant embryos as well as their reduced presence in the OFT. Impaired migration of ASHF progenitors into the heart tube could account for these observations. Alternative explanations would be premature differentiation or increased apoptosis of ISL1+ progenitors in the OFT of the mutant embryos, but they would not account for the increase in cell numbers in the ASHF. Interestingly, defects in the migration of progenitors has also been proposed as the cause of heart defects in zebrafish and murine embryos after reducing the levels of cohesin or its loader NIPBL (Muto et al., 2011; Santos et al., 2016; Schuster et al., 2015). The transcriptomic changes identified in the heart of KO embryos could contribute to this defect, although the underlying cellular and molecular mechanisms need to be identified. Increasing evidence supports the notion that the presence of cohesin-STAG2 at enhancer elements independently of CTCF promotes cell-type-specific transcription, a function that is not compensated by cohesin-STAG1 (Cuadrado et al., 2019; Kojic et al., 2018; Viny et al., 2019). Consistent with this idea, we observed altered tissue-specific transcription patterns in KO embryonic hearts, with a lower expression of cardiac genes and de-repression of genes from other lineages. Thus, we propose that defects in both proliferation and lineage specification contribute to the heart abnormalities observed in the STAG2-deficient embryos. We cannot ascertain whether these heart defects are the primary cause of embryonic death. However, the heart is one of the first organs to start differentiating in the embryo and the first one to become functional (Bruneau, 2013). Impaired heart function would make embryos unable to sustain further development, thus masking defects in other organs arising later.

Cohesinopathy cases with *STAG2* mutations have been reported recently. Male patients display mild phenotypes, lack heart defects, and carry missense variants. In contrast, ventricular septal defects and other heart anomalies have been described in female patients carrying loss-of-function or missense variants (Lehalle et al., 2017; Mullegama et al., 2017, 2019; Soardi et al., 2017; Yuan et al., 2019). Because *STAG2* is an X-linked gene, the embryonic lethality of *Stag2*-null male murine embryos reported here explains why inactivating germline mutations will most likely not be tolerated in males, whereas heterozygous females may survive through the selection of cells in which the WT allele is not silenced by the X inactivation process. Heterozygous female embryos resulting from mating $Stag2^{lox/lox}$ females with *CAG-Cre* males arrive normally to mid-gestation (E12.5), but they are born at sub-Mendelian ratios, indicating problems in the last stages of embryonic development (Figure 4A). Although the heterozygous females that are born appear as healthy as their WT littermates, more specific studies will be required to address the potential resemblance with the phenotypes of female patients carrying heterozygous mutations in *STAG2*.

In summary, here, we show the distinct functional properties of STAG2 at the cellular and organismal levels in mice, compared with those of STAG1. Cells lacking cohesin-STAG2 are viable both *in vitro* (tissue culture) and *in vivo* (in embryos and adult tissues), confirming that cohesin-STAG1 is sufficient to fulfill essential cohesin functions (van der Lelij et al., 2017; Liu et al., 2018). However, their decreased proliferation and altered transcriptomes lead to embryonic lethality, a result that provides further compelling evidence for cell- and tissue-specific roles of the two cohesin complexes and how their dysfunction may contribute to disease. We speculate that genomic changes derived from decreased accuracy of chromosome segregation and/or DNA repair as well as transcriptional alterations affecting cell identity and stem cell physiology may underlie the behavior of *STAG2* mutant tumors. Although inactivation of *Stag2* in adult mice did not increase tumor incidence in our study, similar to other major tumor suppressor genes such as *Cdkn2a* or *Rb* (Krimpenfort et al., 2001; Sharpless et al., 2001; Vooijs and Berns, 1999), these mice will be useful to model the cooperation of *STAG2* mutations with other genetic alterations for promoting tumorigenesis in a wide variety of cell types.

STAR★METHODS

Detailed methods are provided in the online version of this paper and include the following:

- KEY RESOURCES TABLE
- RESOURCE AVAILABILITY
  - Lead Contact
  - Materials Availability
  - Data and Code Availability
- EXPERIMENTAL MODEL AND SUBJECT DETAILS
  - Generation of a conditional knockout allele for Stag2
  - MEFs
- METHOD DETAILS
  - MEF characterization
  - Histopathology and immunohistochemical (IHC) analyses of adult tissue sections
  - Hematological analyses
  - Hematopoietic cell isolation and Flow Cytometry
  - *In vitro* colony-forming unit assays
  - Establishment of intestinal organoids
  - Hematoxylin and immunofluorescence staining of mouse embryo sections
  - RNA-sequencing
- QUANTIFICATION AND STATISTICAL ANALYSIS

SUPPLEMENTAL INFORMATION

Supplemental Information can be found online at https://doi.org/10.1016/j.celrep.2020.108014.

ACKNOWLEDGMENTS

We acknowledge the excellent technical support of the CNIO Mouse Genome Editing unit led by Sagrario Ortega and the CNIC Microscopy unit, in particular Verónica Labrador, as well as the help of Natalia del Pozo, Ana Cuadrado, Dácil Alonso, Alba de Martino, Eduardo Caleiras, and Cristian Perna. This work has been supported by the State Research Agency (AEI), Spanish Ministry of Science and Innovation, with cofunding of the European Regional Development Funds (grants BFU2013-48481-R and BFU2016-79841-R to A.L., SAF2015-70553-R to F.X.R., BFU2017-84914-P and BFU2015-72319-EXP to M.M., and BES-2014-069166 fellowship to M.D.K.), and a grant to F.X.R. and a Postdoctoral Contract to E.L. from the Fundación Científica de la Asociación Española Contra el Cáncer. Both CNIO and CNIC are supported by Instituto de Salud Carlos III (ISCIII) and Severo Ochoa Centers of Excellence

(SEV-2015-0510 and SEV-2015-0505). The CNIC is also supported by the Pro CNIC Foundation.

AUTHOR CONTRIBUTIONS

E.L. and M.R.-C. generated the *Stag2* cKO mouse; M.D.K. characterized MEFs; E.L., E.A., and I.C. carried out the studies in adult mice; M.D.K. and C.B.-C. performed the embryo studies; D.G.-L. analyzed RNA-seq data; A.H., M.M., F.X.R., and A.L. supervised the study and contributed to experimental design and data interpretation.

DECLARATION OF INTERESTS

The authors declare no competing interests

Received: March 30, 2020
Revised: June 15, 2020
Accepted: July 17, 2020
Published: August 11, 2020

REFERENCES

Balbás-Martínez, C., Sagrera, A., Carrillo-de-Santa-Pau, E., Earl, J., Márquez, M., Vazquez, M., Lapi, E., Castro-Giner, F., Beltran, S., Bayés, M., et al. (2013). Recurrent inactivation of STAG2 in bladder cancer is not associated with aneuploidy. Nat. Genet. *45*, 1464–1469.

Belteki, G., Haigh, J., Kabacs, N., Haigh, K., Sison, K., Costantini, F., Whitsett, J., Quaggin, S.E., and Nagy, A. (2005). Conditional and inducible transgene expression in mice through the combinatorial use of Cre-mediated recombination and tetracycline induction. Nucleic Acids Res. *33*, e51.

Bruneau, B.G. (2013). Signaling and transcriptional networks in heart development and regeneration. Cold Spring Harb. Perspect. Biol. *5*, a008292.

Cai, C.-L., Liang, X., Shi, Y., Chu, P.-H., Pfaff, S.L., Chen, J., and Evans, S. (2003). Isl1 identifies a cardiac progenitor population that proliferates prior to differentiation and contributes a majority of cells to the heart. Dev. Cell *5*, 877–889.

Canudas, S., and Smith, S. (2009). Differential regulation of telomere and centromere cohesion by the Scc3 homologues SA1 and SA2, respectively, in human cells. J. Cell Biol. *187*, 165–173.

Carretero, M., Ruiz-Torres, M., Rodríguez-Corsino, M., Barthelemy, I., and Losada, A. (2013). Pds5B is required for cohesion establishment and Aurora B accumulation at centromeres. EMBO J. *32*, 2938–2949.

Cuadrado, A., and Losada, A. (2020). Specialized functions of cohesins STAG1 and STAG2 in 3D genome architecture. Curr. Opin. Genet. Dev. *61*, 9–16.

Cuadrado, A., Remeseiro, S., Graña, O., Pisano, D.G., and Losada, A. (2015). The contribution of cohesin-SA1 to gene expression and chromatin architecture in two murine tissues. Nucleic Acids Res. *43*, 3056–3067.

Cuadrado, A., Giménez-Llorente, D., Kojic, A., Rodríguez-Corsino, M., Cuartero, Y., Martín-Serrano, G., Gómez-López, G., Marti-Renom, M.A., and Losada, A. (2019). Specific Contributions of Cohesin-SA1 and Cohesin-SA2 to TADs and Polycomb Domains in Embryonic Stem Cells. Cell Rep. *27*, 3500–3510.e4.

De Koninck, M., and Losada, A. (2016). Cohesin mutations in cancer. Cold Spring Harb. Perspect. Med. *6*, a026476.

Dowen, J.M., Fan, Z.P., Hnisz, D., Ren, G., Abraham, B.J., Zhang, L.N., Weintraub, A.S., Schujiers, J., Lee, T.I., Zhao, K., and Young, R.A. (2014). Control of cell identity genes occurs in insulated neighborhoods in mammalian chromosomes. Cell *159*, 374–387.

Faure, A.J., Schmidt, D., Watt, S., Schwalie, P.C., Wilson, M.D., Xu, H., Ramsay, R.G., Odom, D.T., and Flicek, P. (2012). Cohesin regulates tissue-specific expression by stabilizing highly occupied cis-regulatory modules. Genome Res. *22*, 2163–2175.

Hay, T., Patrick, T., Winton, D., Sansom, O.J., and Clarke, A.R. (2005). Brca2 deficiency in the murine small intestine sensitizes to p53-dependent apoptosis and leads to the spontaneous deletion of stem cells. Oncogene *24*, 3842–3846.

Ibarra-Soria, X., Jawaid, W., Pijuan-Sala, B., Ladopoulos, V., Scialdone, A., Jörg, D.J., Tyser, R.C.V., Calero-Nieto, F.J., Mulas, C., Nichols, J., et al. (2018). Defining murine organogenesis at single-cell resolution reveals a role for the leukotriene pathway in regulating blood progenitor formation. Nat. Cell Biol. *20*, 127–134.

Ireland, H., Kemp, R., Houghton, C., Howard, L., Clarke, A.R., Sansom, O.J., and Winton, D.J. (2004). Inducible Cre-mediated control of gene expression in the murine gastrointestinal tract: effect of loss of β-catenin. Gastroenterology *126*, 1236–1246.

Kagey, M.H., Newman, J.J., Bilodeau, S., Zhan, Y., Orlando, D.A., van Berkum, N.L., Ebmeier, C.C., Goossens, J., Rahl, P.B., Levine, S.S., et al. (2010). Mediator and cohesin connect gene expression and chromatin architecture. Nature *467*, 430–435.

Keeley, T.M., Horita, N., and Samuelson, L.C. (2019). Tamoxifen-Induced Gastric Injury: Effects of Dose and Method of Administration. Cell. Mol. Gastroenterol. Hepatol. *8*, 365–367.

Kelly, R.G., Buckingham, M.E., and Moorman, A.F. (2014). Heart fields and cardiac morphogenesis. Cold Spring Harb. Perspect. Med. *4*, a015750.

Khaminets, A., Ronnen-Oron, T., Baldauf, M., Meier, E., and Jasper, H. (2020). Cohesin controls intestinal stem cell identity by maintaining association of Escargot with target promoters. eLife *9*, e48160.

Kim, J.S., He, X., Orr, B., Wutz, G., Hill, V., Peters, J.M., Compton, D.A., and Waldman, T. (2016). Intact Cohesion, Anaphase, and Chromosome Segregation in Human Cells Harboring Tumor-Derived Mutations in STAG2. PLoS Genet. *12*, e1005865.

Kojic, A., Cuadrado, A., De Koninck, M., Giménez-Llorente, D., Rodríguez-Corsino, M., Gómez-López, G., Le Dily, F., Marti-Renom, M.A., and Losada, A. (2018). Distinct roles of cohesin-SA1 and cohesin-SA2 in 3D chromosome organization. Nat. Struct. Mol. Biol. *25*, 496–504.

Kong, X., Ball, A.R., Jr., Pham, H.X., Zeng, W., Chen, H.Y., Schmiesing, J.A., Kim, J.S., Berns, M., and Yokomori, K. (2014). Distinct functions of human cohesin-SA1 and cohesin-SA2 in double-strand break repair. Mol. Cell. Biol. *34*, 685–698.

Krimpenfort, P., Quon, K.C., Mooi, W.J., Loonstra, A., and Berns, A. (2001). Loss of p16Ink4a confers susceptibility to metastatic melanoma in mice. Nature *413*, 83–86.

Lambert, J.F., Benoit, B.O., Colvin, G.A., Carlson, J., Delville, Y., and Quesenberry, P.J. (2000). Quick sex determination of mouse fetuses. J. Neurosci. Methods *95*, 127–132.

Lawrence, M.S., Stojanov, P., Mermel, C.H., Robinson, J.T., Garraway, L.A., Golub, T.R., Meyerson, M., Gabriel, S.B., Lander, E.S., and Getz, G. (2014). Discovery and saturation analysis of cancer genes across 21 tumour types. Nature *505*, 495–501.

Lehalle, D., Mosca-Boidron, A.-L., Begtrup, A., Boute-Benejean, O., Charles, P., Cho, M.T., Clarkson, A., Devinsky, O., Duffourd, Y., Duplomb-Jego, L., et al. (2017). *STAG1* mutations cause a novel cohesinopathy characterised by unspecific syndromic intellectual disability. J. Med. Genet. *54*, 479–488.

Liu, J., Zhang, Z., Bando, M., Itoh, T., Deardorff, M.A., Clark, D., Kaur, M., Tandy, S., Kondoh, T., Rappaport, E., et al. (2009). Transcriptional dysregulation in NIPBL and cohesin mutant human cells. PLoS Biol. *7*, e1000119.

Liu, Y., Xu, H., Van der Jeught, K., Li, Y., Liu, S., Zhang, L., Fang, Y., Zhang, X., Radovich, M., Schneider, B.P., et al. (2018). Somatic mutation of the cohesin complex subunit confers therapeutic vulnerabilities in cancer. J. Clin. Invest. *128*, 2951–2965.

Losada, A., Yokochi, T., Kobayashi, R., and Hirano, T. (2000). Identification and characterization of SA/Scc3p subunits in the Xenopus and human cohesin complexes. J. Cell Biol. *150*, 405–416.

Love, M.I., Huber, W., and Anders, S. (2014). Moderated estimation of fold change and dispersion for RNA-seq data with DESeq2. Genome Biol. *15*, 550.

Meisenberg, C., Pinder, S.I., Hopkins, S.R., Wooller, S.K., Benstead-Hume, G., Pearl, F.M.G., Jeggo, P.A., and Downs, J.A. (2019). Repression of

Transcription at DNA Breaks Requires Cohesin throughout Interphase and Prevents Genome Instability. Mol. Cell *73*, 212–223.e7.

Merkenschlager, M., and Nora, E.P. (2016). CTCF and Cohesin in Genome Folding and Transcriptional Gene Regulation. Annu. Rev. Genomics Hum. Genet. *17*, 17–43.

Mondal, G., Stevers, M., Goode, B., Ashworth, A., and Solomon, D.A. (2019). A requirement for STAG2 in replication fork progression creates a targetable synthetic lethality in cohesin-mutant cancers. Nat. Commun. *10*, 1686.

Morales, C., and Losada, A. (2018). Establishing and dissolving cohesion during the vertebrate cell cycle. Curr. Opin. Cell Biol. *52*, 51–57.

Mullegama, S.V., Klein, S.D., Mulatinho, M.V., Senaratne, T.N., Singh, K., UCLA Clinical Genomics Center; Nguyen, D.C., Gallant, N.M., Strom, S.P., Ghahremani, S., Rao, N.P., and Martinez-Agosto, J.A. (2017). De novo loss-of-function variants in STAG2 are associated with developmental delay, microcephaly, and congenital anomalies. Am. J. Med. Genet. A. *173*, 1319–1327.

Mullegama, S.V., Klein, S.D., Signer, R.H., UCLA Clinical Genomics Center; Vilain, E., and Martinez-Agosto, J.A. (2019). Mutations in *STAG2* cause an X-linked cohesinopathy associated with undergrowth, developmental delay, and dysmorphia: Expanding the phenotype in males. Mol. Genet. Genomic Med. *7*, e00501.

Mullenders, J., Aranda-Orgilles, B., Lhoumaud, P., Keller, M., Pae, J., Wang, K., Kayembe, C., Rocha, P.P., Raviram, R., Gong, Y., et al. (2015). Cohesin loss alters adult hematopoietic stem cell homeostasis, leading to myeloproliferative neoplasms. J. Exp. Med. *212*, 1833–1850.

Muto, A., Calof, A.L., Lander, A.D., and Schilling, T.F. (2011). Multifactorial origins of heart and gut defects in nipbl-deficient zebrafish, a model of Cornelia de Lange Syndrome. PLoS Biol. *9*, e1001181.

Nasmyth, K., and Haering, C.H. (2009). Cohesin: its roles and mechanisms. Annu. Rev. Genet. *43*, 525–558.

Park, E.J., Ogden, L.A., Talbot, A., Evans, S., Cai, C.-L., Black, B.L., Frank, D.U., and Moon, A.M. (2006). Required, tissue-specific roles for Fgf8 in outflow tract formation and remodeling. Development *133*, 2419–2433.

Remeseiro, S., Cuadrado, A., Carretero, M., Martínez, P., Drosopoulos, W.C., Cañamero, M., Schildkraut, C.L., Blasco, M.A., and Losada, A. (2012a). Cohesin-SA1 deficiency drives aneuploidy and tumourigenesis in mice due to impaired replication of telomeres. EMBO J. *31*, 2076–2089.

Remeseiro, S., Cuadrado, A., Gómez-López, G., Pisano, D.G., and Losada, A. (2012b). A unique role of cohesin-SA1 in gene regulation and development. EMBO J. *31*, 2090–2102.

Ruzankina, Y., Pinzon-Guzman, C., Asare, A., Ong, T., Pontano, L., Cotsarelis, G., Zediak, V.P., Velez, M., Bhandoola, A., and Brown, E.J. (2007). Deletion of the developmentally essential gene ATR in adult mice leads to age-related phenotypes and stem cell loss. Cell Stem Cell *1*, 113–126.

Santos, R., Kawauchi, S., Jacobs, R.E., Lopez-Burks, M.E., Choi, H., Wikenheiser, J., Hallgrimsson, B., Jamniczky, H.A., Fraser, S.E., Lander, A.D., and Calof, A.L. (2016). Conditional Creation and Rescue of Nipbl-Deficiency in Mice Reveals Multiple Determinants of Risk for Congenital Heart Defects. PLoS Biol. *14*, e2000197.

Sarogni, P., Pallotta, M.M., and Musio, A. (2020). Cornelia de Lange syndrome: from molecular diagnosis to therapeutic approach. J. Med. Genet. *57*, 289–295.

Sasca, D., Yun, H., Giotopoulos, G., Szybinski, J., Evan, T., Wilson, N.K., Gerstung, M., Gallipoli, P., Green, A.R., Hills, R., et al. (2019). Cohesin-dependent regulation of gene expression during differentiation is lost in cohesin-mutated myeloid malignancies. Blood *134*, 2195–2208.

Schuster, K., Leeke, B., Meier, M., Wang, Y., Newman, T., Burgess, S., and Horsfield, J.A. (2015). A neural crest origin for cohesinopathy heart defects. Hum. Mol. Genet. *24*, 7005–7016.

Sharpless, N.E., Bardeesy, N., Lee, K.H., Carrasco, D., Castrillon, D.H., Aguirre, A.J., Wu, E.A., Horner, J.W., and DePinho, R.A. (2001). Loss of p16Ink4a with retention of p19Arf predisposes mice to tumorigenesis. Nature *413*, 86–91.

Sinha, T., Li, D., Théveniau-Ruissy, M., Hutson, M.R., Kelly, R.G., and Wang, J. (2015). Loss of Wnt5a disrupts second heart field cell deployment and may contribute to OFT malformations in DiGeorge syndrome. Hum. Mol. Genet. *24*, 1704–1716.

Soardi, F.C., Machado-Silva, A., Linhares, N.D., Zheng, G., Qu, Q., Pena, H.B., Martins, T.M.M., Vieira, H.G.S., Pereira, N.B., Melo-Minardi, R.C., et al. (2017). Familial *STAG2* germline mutation defines a new human cohesinopathy. NPJ Genom. Med. *2*, 7.

Taylor, C.F., Platt, F.M., Hurst, C.D., Thygesen, H.H., and Knowles, M.A. (2014). Frequent inactivating mutations of STAG2 in bladder cancer are associated with low tumour grade and stage and inversely related to chromosomal copy number changes. Hum. Mol. Genet. *23*, 1964–1974.

Thol, F., Bollin, R., Gehlhaar, M., Walter, C., Dugas, M., Suchanek, K.J., Kirchner, A., Huang, L., Chaturvedi, A., Wichmann, M., et al. (2014). Mutations in the cohesin complex in acute myeloid leukemia: clinical and prognostic implications. Blood *123*, 914–920.

Tsuchihashi, T., Maeda, J., Shin, C.H., Ivey, K.N., Black, B.L., Olson, E.N., Yamagishi, H., and Srivastava, D. (2011). Hand2 function in second heart field progenitors is essential for cardiogenesis. Dev. Biol. *351*, 62–69.

van der Lelij, P., Lieb, S., Jude, J., Wutz, G., Santos, C.P., Falkenberg, K., Schlattl, A., Ban, J., Schwentner, R., Hoffmann, T., et al. (2017). Synthetic lethality between the cohesin subunits *STAG1* and *STAG2* in diverse cancer contexts. eLife *6*, e26980.

Viny, A.D., Bowman, R.L., Liu, Y., Lavallée, V.-P., Eisman, S.E., Xiao, W., Durham, B.H., Navitski, A., Park, J., Braunstein, S., et al. (2019). Cohesin Members Stag1 and Stag2 Display Distinct Roles in Chromatin Accessibility and Topological Control of HSC Self-Renewal and Differentiation. Cell Stem Cell *25*, 682–696.e8.

Vooijs, M., and Berns, A. (1999). Developmental defects and tumor predisposition in Rb mutant mice. Oncogene *18*, 5293–5303.

Wutz, G., Ladurner, R., St Hilaire, B.G., Stocsits, R.R., Nagasaka, K., Pignard, B., Sanborn, A., Tang, W., Várnai, C., Ivanov, M.P., et al. (2020). ESCO1 and CTCF enable formation of long chromatin loops by protecting cohesin^{STAG1} from WAPL. eLife *9*, e52091.

Yuan, B., Neira, J., Pehlivan, D., Santiago-Sim, T., Song, X., Rosenfeld, J., Posey, J.E., Patel, V., Jin, W., Adam, M.P., et al. (2019). Clinical exome sequencing reveals locus heterogeneity and phenotypic variability of cohesinopathies. Genet. Med. *21*, 663–675.

STAR★METHODS

KEY RESOURCES TABLE

REAGENT or RESOURCE	SOURCE	IDENTIFIER
Antibodies		
MEK2 mouse monoclonal	BD	Cat# M24520
Rad21 rabbit polyclonal	Carretero et al., 2013	N/A
STAG1 rat monoclonal	Kojic et al., 2018	N/A
STAG1 rabbit polyclonal	Remeseiro et al., 2012a	N/A
STAG2 mouse monoclonal	SCBT	Cat# SC-81852; RRID:AB_2199948
BrdU-FITC	BD	Cat# 556028; RRID:AB_396304
Lineage cocktail	BD	Cat# 558451
Ly-6A/E (Sca-1)-PE-Cy7	BD	Cat# 558162; RRID:AB_647253
CD117 (c-kit)-PerCP-Cy5.5	BioLegend	Cat# 105824; RRID:AB_2131597
CD48-APC-Cy7	BioLegend	Cat# 103432; RRID:AB_2561463
CD150 (SLAM)-BV510	BioLegend	Cat# 115929; RRID:AB_2562189
CD34-e Fluor 660	eBioscience	Cat# 50034182; RRID:AB_10596826
CD16/32- BV605	BD	Cat# 563006; RRID:AB_2737947
CD11b (Mac1)-PE-Cy7	BioLegend	Cat# 101216; RRID:AB_312799
Ly6G-Dylight 450; conjugated in house	BioXcell	N/A
CD3ε- PerCP-Cy5.5	BioLegend	Cat# 100328; RRID:AB_893318
CD45R (B220)-APC-Cy7	BD	Cat# 552094; RRID:AB_394335
Streptavidin DyLight 405	Jackson Immunoresearch	Cat# 016-470-084; RRID:AB_2337248
Ter119-Pacific Blue	BioLegend	Cat# 116231; RRID:AB_2149212
BrdU (MoBu-1)	Santa Cruz	Cat# 51514; RRID:AB_626519
Cleaved-caspase3 (ASP175)	Cell Signaling	Cat# 9661; RRID:AB_2341188)
H3P rabbit polyclonal	Millipore	Cat# 06-570; RRID:AB_310177
ISL1 mouse monoclonal	DSHB Hybridoma Bank	Cat# 39.4D5; RRID:AB_2314683
Chemicals, Peptides, and Recombinant Proteins		
Prolong Gold Antifade Reagent	Life Technologies	Cat# P36930
Matrigel	Corning	Cat# 356231
Cell recovery solution	Corning	Cat# 354253
Dispase II solution	GIBCO	Cat# 17105041
Formalin	Sigma	Cat# HT501128-4L
Biotin-16-dUTP	Roche	Cat# 11093070910
TRI reagent	Sigma	Cat# T9424
Critical Commercial Assays		
Cytofix/Cytoperm kit	BD	Cat# 554722
FITC Active Caspase-3 Apoptosis kit	BD	Cat# 550480
Terminal Transferase recombinant kit	Roche	Cat# 03333574001
Deposited Data		
RNA-seq datasets in mouse embryos	This paper	GEO: GSE152298
Experimental Models: Organisms/Strains		
Stag2 conditional knockout mice	This paper	N/A
Tg.hUBC-CreERT2 mice	Ruzankina et al., 2007	N/A
Tg.CAG-Cre mice	Belteki et al., 2005	N/A
Oligonucleotides		
Primer Stag2 f1: TGGTGCTTGGGATCAGATTT	This paper	N/A
Primer Stag2 r1: TCCCTCATCAAAGTCGAAAA	This paper	N/A

(*Continued on next page*)

Continued

REAGENT or RESOURCE	SOURCE	IDENTIFIER
Primer Stag2 r2: AACAGCCTGAGCAAAGAATCC	This paper	N/A
Primer Sry fwd: TGGGACTGGTGACAATTGTC	Lambert et al., 2000	N/A
Primer Sry rev: GAGTACAGGTGTGCAGCTCT	Lambert et al., 2000	N/A
Recombinant DNA		
Stag2 targeting vector	EUCOMM	PG00032_A_D11-3
Software and Algorithms		
GraphPad Prism (statistical analysis)	GraphPad Software Inc	https://www.graphpad.com/scientific-software/prism/
Flow Jo v10.0.8 (flow cytometry analysis)	Flow Jo LLC	https://www.flowjo.com/solutions/flowjo
LAS AF v3.8 (imaging)	Leica	https://www.leica-microsystems.com/products/microscope-software/p/leica-application-suite/
Definiens Developer XD v2.5 (imaging)	Definiens Inc – AstraZeneca	N/A
NIS Elements D3.2 and 4.30 (imaging)	Nikon	https://www.microscope.healthcare.nikon.com/products/software/nis-elements
FIJI v1.52b		https://imagej.net/Fiji
Lexogen Quantseq pipeline (RNA-seq analysis)	BlueBee	https://www.lexogen.com/store/quantseq-data-analysis-bluebee-platform/
DESeq2 (RNA-seq analysis)	Love et al., 2014	http://www.bioconductor.org/packages/release/bioc/html/DESeq2.html

RESOURCE AVAILABILITY

Lead Contact

Further information and requests for resources and reagents should be directed to and will be fulfilled by the Lead Contact, Ana Losada (alosada@cnio.es).

Materials Availability

Resources generated in this study are available upon request. Requests of *Stag2* cKO mice should be addressed to A. Losada (alosada@cnio.es).

Data and Code Availability

RNA-sequencing datasets have been deposited in the Gene Expression Omnibus (GEO) under the accession number GSE152298

EXPERIMENTAL MODEL AND SUBJECT DETAILS

Generation of a conditional knockout allele for Stag2

The targeting vector PG00032_A_D11-3 (EUCOMM) containing loxP sites flanking exon 7 of the *Stag2* gene and a SA-lacZ-Neo cassette flanked by FRT sites integrated in intron 6 was electroporated into G4 mouse embryonic stem cells (Figure S1A). Clones were selected in G418 and screened by Southern blotting for homologous recombination (Figure S1B). Positive clones were infected with adeno-FLP to remove the selection cassette and create the conditional allele and microinjected into C57BL/6BrdCrHsd-Tyr morulae. Germline transmitting chimeras were screened by PCR (primers f1: 5′-TGGTGCTTGGGATCAGATTT-3′ and r1: 5′-TCCCTCATCAAAGTCGAAAA-3′) and selected to generate the colonies (Figure S1C). Mice carrying the *Stag2* cKO allele were crossed with mice carrying a tamoxifen inducible Cre-ERT2 allele (*Tg.hUBC-CreERT2)* for MEF isolation and adult mice viability assays or with a constitutively active Cre (*Tg.CAG-Cre)* to assess embryonic development and lethality (Figure S1D). All crosses were maintained in a predominantly C57BL/6 background. To induce recombination in adult animals, 4 week-old mice were fed for variable periods of time with a TMX-containing diet, as specified. For the experiments in adult animals, both male and female mice were analyzed. For experiments in embryos, only male embryos were used, as explained in main text. All animal procedures were approved by local and regional ethics committees (Institutional Animal Care and Use Committee and Ethics Committee for Research and Animal Welfare, Instituto de Salud Carlos III) and performed according to the European Union guidelines.

MEFs

MEFs were isolated from E12.5 embryos resulting from mating *Stag2*$^{lox/lox}$ females with *Tg.hUBC-CreERT2*$^{+/T}$ males and genotyped for *Stag2* (with a mixture of primers f1, r1 and r2: 5′- AACAGCCTGAGCAAAGAATCC-3′), *CreERT2* (fwd: 5′- TGAAGCTCCGGTTTT GAACT-3′; rev: 5′- GGTTCTTGCGAACCTCATCAC-3′) and the *Sry* Y chromosome marker (fwd: 5′-TGGGACTGGTGACAATTGTC-3′: rev: 5′- GAGTACAGGTGTGCA GCTCT-3′). MEFs were cultured in DMEM supplemented with 20% FBS and 1% penicillin-streptomycin and grown at 37°C under 90% humidity and 5% CO_2.

METHOD DETAILS

MEF characterization

For each experiment, MEFs derived from 2-4 different embryos were analyzed. To ablate STAG2 expression, conditional *Stag2*$^{lox/Y}$;*CreERT2*$^{+/T}$ MEFs were cultured in the presence of 1 μM 4-hydroxy tamoxifen (4-OHT) for 3-4 days and the efficiency of depletion was assessed by immunoblotting. The same cells cultured without 4-OHT served as control.

To assess proliferation, MEFs pretreated for 4 days with 4-OHT were seeded at low confluence in multiwell plates (3 wells per time point). In the following days, cells were collected and counted in a Neubauer hemocytometer.

For cell cycle analysis, MEFs grown for 4 days in medium with or without 4-OHT were collected after a 30 min pulse with 30 μM BrdU, fixed and incubated with a FITC-conjugated anti-BrdU antibody and DNA was stained with 50 μg/ml propidium iodide. To study apoptosis, MEFs grown for 4 days in the presence of 4-OHT were collected (both adhered and floating cells) and fixed and permeabilized using the BD Cytofix/Cytoperm kit (BD 554722). Cells stained with DAPI and the FITC Active Caspase-3 Apoptosis kit (BD 550480) according to manufacturer instructions. Flow cytometry was performed in a FACS Canto II cytometer and profiles were analyzed using FlowJo 10.0.8 software.

For analysis of mitotic defects, MEFs were serum-starved (0.1% FBS) for 3 days in the presence or absence of 4-OHT, switched to medium supplemented with 20% FBS, and collected after 36 h. For chromosome spreads, 0.1 μg/ml colcemid was added to the medium 3-4 h before harvesting. Cells were swollen in 0.03 M sodium citrate, fixed in methanol:acetic acid 3:1 and dropped onto slides. For anaphase analysis, cells were seeded onto coverslips at the time of release from G0 arrest. In both cases, cells were stained with 1 μg/ml DAPI, mounted with Vectashield and imaged using a Leica DM6000 microscope with LAS AF software.

Histopathology and immunohistochemical (IHC) analyses of adult tissue sections

Tissues from adult mice were analyzed following standard histopathology procedures. Mice were sacrificed by cervical dislocation and a complete necropsy was performed; the following tissues were analyzed histologically: bladder, pancreas and associated lymph nodes, spleen, kidney, liver, lung, heart, brain, gastrointestinal tract, thymus, thyroid and parathyroid. WT littermates were sacrificed and used as controls. Organs were fixed in 4% neutral buffered (pH 6.9) formaldehyde for 24 h and embedded in paraffin. After standard H-E staining, sections were analyzed in a Leica DM5000B microscope by a trained veterinary pathologist and histological findings were recorded. After scanning of histological slides (AxioScan 4.1, Zeiss), representative microphotographs were taken.

IHC was performed on 2.5-μm sections of formalin-fixed paraffin-embedded tissues, unless otherwise indicated. After deparaffinization and rehydration, antigen retrieval was performed by boiling in citrate buffer pH 6 for 10 min and endogenous peroxidase was inactivated with 3% H_2O_2–methanol for 30 min at room temperature (RT). Sections were blocked with 2% BSA in PBS and incubated with anti-STAG2 and anti-cleaved caspase-3 (Asp175). After washing, the Envision secondary reagent (DAKO) was added for 40 min at RT and sections were washed three times with PBS. 3,3′-Diaminobenzidine tetrahydrochloride (DAB) was used as a chromogen. Sections were lightly counterstained with hematoxylin, dehydrated and mounted. A non-related IgG was used as a negative control. STAG2 expression in sections of liver, pancreas, brain, spleen and intestine of KO mice was assessed by IHC at 12, 24, 35 and 60 weeks of age. Representative microphotographs were taken and quantified with ImageJ software. For IF, after deparaffinization, rehydration and antigen retrieval, sections were incubated with 3% BSA/0.1% Triton in PBS for 45 min at room temperature and incubated with primary anti-BrdU overnight at 4°C. After washing with 0.1% Triton/PBS, an Alexa Fluor 555-labeled goat anti-rabbit Ig secondary antibody was added for 45 min, sections were washed, and nuclei were counterstained with DAPI. After washing with PBS, sections were mounted with Prolong Gold Antifade Reagent (Life Technologies, P36930). Images were acquired using a confocal microscope (Leica, SP5).

Hematological analyses

Peripheral blood was extracted from the mouse cheek and collected in EDTA-coated tubes. Standard complete blood counts were performed using an automated analyzer (Abacus Junior Vet, CVM Diagnóstico Veterinario S.L, Navarra, Spain) according to the manufacturers' instructions. For the GFP/Tomato blood competition experiment, KO mice received a TMX diet from weaning and blood was collected at 8, 12, 16, 20, 24 weeks of age. After RBC depletion using hypotonic lysis buffer, GFP or Tomato positive cells were quantified on a LSRII Fortessa (BD and analyzed with FlowJo v10 software (Tree Star, Ashland, OR).

Hematopoietic cell isolation and Flow Cytometry

Bone marrow was isolated from the tibia and femur; peripheral blood was obtained by cardiac puncture; spleens were disaggregated and homogenized through a 70-μm strainer; all these samples were incubated for 10 min in RBC lysis buffer and resuspended in PBS. For the analysis of LSK and MPs, cells were incubated with the biotinylated lineage antibody cocktail (CD3e, B220, CD11b, Gr1 and Ter119), together with streptavidin conjugated to DyLight 405, anti-Sca-1 (D7) -PE-Cy7 (BD), and anti- c-Kit (2B8) -PerCP-Cy5.5 for 30 min. For the analysis of myeloid progenitors, cells were incubated with the previous antibodies plus anti-CD34 -eF660 (RAM34) and anti-FcγRII/III - BV605 (2.4G2). For the analysis of bone marrow Ter119+ cells, cells were incubated with anti-Ter119-Pacific Blue for 15 min. For the analysis of peripheral blood leukocytes (PBL) and splenocytes, cells were stained with anti-Ly6G -DyLight 405 (1A8, in-house conjugated), anti-B220 labeled with APCCy7 (RA3-6B2), and anti-Cd11b -PECy7 (Mac1) and anti-CD3e -PerCP-Cy5.5 (145-2C11) for 15 min. Samples were collected on a LSRII Fortessa (BD) and analyzed with FlowJo v10 software (Tree Star, Ashland, OR).

In vitro colony-forming unit assays

To evaluate self-renewal capacity, 20,000 Tomato or GFP^+ bone marrow cells from *Stag2* KO mice were FACS-sorted, seeded in cytokine-supplemented methylcellulose tubes, and plated in duplicates in 35 mm culture dishes (NUNC A/S; Roskilde, Denmark). Cultures were incubated at 37°C in a 5% CO_2 atmosphere. The number of CFU-Cs was scored on day 7 using an inverted microscope. Cells were sorted with a FACSAria Instrument (BD).

Establishment of intestinal organoids

Small intestines of 8 week-old mice were opened longitudinally, washed with cold PBS supplemented with antibiotics and gently scraped to remove villi. The tissue was chopped into around 5 mm pieces, further washed with cold PBS and antibiotic and incubated in 8 mM EDTA with PBS for 5 min at RT and then for 30 min on ice. Tissue fragments were vigorously shaken with cold PBS. The supernatant was enriched for crypts. This procedure was repeated twice and the supernatant joined. This fraction was passed through a 70-μm cell strainer (BD Bioscience) to remove residual villous material. Isolated crypts were centrifuged at 800 rpm for 3 min to separate crypts from single cells. The final fraction consisted of essentially pure crypts and was embedded in in growth factor-reduced and phenol red-free Matrigel (Corning, 356231). Matrigel-crypts suspensions (20 μL drops) were plated onto 6-well plates, allowed to settle in a humidified incubator at 37°C/5% CO_2, and overlaid with 2 mL of culture medium (Advanced DMEM/F12 (Invitrogen)) containing growth factors (50ng/ml EGF (Peprotech), 500 ng/ml R-spondin (Sigma) and 100 ng/ml Noggin (Peprotech)). Isolated crypts were allowed to close in culture medium for 2-4 days. For sorting experiments, Matrigel was removed with Cell Recovery Solution (Corning, 354253) on ice and the cell suspension was washed with PBS, then with washing medium, and centrifuged at 1200 rpm for 5 min at 4°C. Then, sealed crypts were digested with Dispase II solution (10 mg/mL) (GIBCO, 17105041) for 15-20 min in a rotating wheel at room temperature. The digestion was stopped with 2 mM EDTA and single cells were obtained by mechanical disruption with a syringe with a 21G needle. Dissociated cells were passed through cell strainer and single, viable ($DAPI^-$), GFP^+ or $Tomato^+$ cells were sorted by flow cytometry using an FACS AriaII (BD Biosciences). Sorted cells were collected in crypt culture medium and embedded in Matrigel in 96-well plates (5000 cells/well) for the clonal growth experiments. Organoids were allowed to grow for 7 days and images were acquired with a CCD-microscope. Three microphotographs in the Z axis were taken in order to collect the majority of the organoids. Then, a Z stack was done using ImageJ software. Quantification was performed with tailored routines programmed in Definiens XD v2.5 software.

Hematoxylin and immunofluorescence staining of mouse embryo sections

Whole-mount embryos were dissected in PBS at RT and imaged using a Leica MZ10F microscope and LAS 3.8 software. DNA from yolk sacs was used to genotype for *Stag2* and *Sry*. Embryos were fixed in 10% formalin solution at pH 7 (Sigma HT501128-4L) overnight at 4°C, dehydrated in an ethanol series and stored in ethanol 70% at 4°C until further processing. Embryos were embedded in paraffin and sectioned transversely at 5-μm. H-E staining was performed by standard procedures [WT1 (n = 3), KO mild (n = 4), WT2 (n = 3) and KO severe (n = 2) at E9.5; WT (n = 3) and KO (n = 3) at E10.5]. Sections were imaged with a Nikon Eclipse 90i microscope and NIS Elements D 3.2 imaging software.

Co-immunostaining for H3P-ISL1-TUNEL was performed using 4 embryos per genotype (WT1, KO mild and WT2). For TUNEL, the Terminal Transferase recombinant kit (Roche 03 333 574 001) and biotin-16-dUTP (Roche 11 093 070 910) were used. Sections were imaged with a Nikon A1R confocal microscope and NIS Elements 4.30 software. H3P signal was quantified with a custom-made ImageJ macro, taking into account both late G2 and M-phase signals. Statistical significance was determined by Kruskal-Wallis test and Dunn's Multiple Comparison post-test using GraphPad Prism 5.03.

RNA-sequencing

Whole mount KO and WT embryos at E9.5 (21-23 pairs of somites) were placed in cold PBS. The whole heart along with surrounding SHF regions and a section of heart-proximal neural tube were dissected, snap-frozen and stored at −80°C. Per genotype and region, 3 replicates were prepared pooling material from 3 embryos that were processed with TRI reagent (Sigma T9424) and homogenized with syringe and needle (25-30G). Chloroform and phase lock tubes (QuantaBio 2302830) were used for phase separation and a subsequent precipitation with ethanol was performed at −20°C. RNA samples were analyzed using a Bioanalyzer 2100 (Agilent) and the

RNA 6000 Pico kit. Libraries were prepared using the QuantSeq 3′ mRNA-seq Library Prep Kit FWD (Lexogen) and sequenced on an Illumina HiSeq 2500 platform. For alignment and gene counting, we applied the Lexogen QuantSeq 2.2.3 pipeline provided by BlueBee, designed for use with the libraries described above. We decided to remove one of the WT heart replicates due to initial inferior RNA integrity and a failure to cluster with the rest of the WT heart samples. The differential expression analyses have been performed with DeSeq2, excluding genes with no reads in any of the samples. Results were filtered by p value < 0.05 and FDR < 0.05. In the heatmaps, color intensities correspond to the relative expression levels for each gene among conditions, normalized using the mean and standard deviation.

QUANTIFICATION AND STATISTICAL ANALYSIS

Information about sample size and statistical test applied for each experiment can be found in the figure legends and in the Method Details section. Difference between groups was defined as significant when $p < 0.05$.